# Attribute expression of fault-controlled karst — Fort Worth Basin, Texas: A tutorial

Jie Qi[1], Bo Zhang[1], Huailai Zhou[1], and Kurt Marfurt[1]

## Abstract

Much of seismic interpretation is based on pattern recognition, such that experienced interpreters are able to extract subtle geologic features that a new interpreter may easily overlook. Seismic pattern recognition is based on the identification of changes in (1) amplitude, (2) phase, (3) frequency, (4) dip, (5) continuity, and (6) reflector configuration. Seismic attributes, which providing quantitative measures that can be subsequently used in risk analysis and data mining, partially automate the pattern recognition problem by extracting key statistical, geometric, or kinematic components of the 3D seismic volume. Early attribute analysis began with recognition of bright spots and quickly moved into the mapping of folds, faults, and channels. Although a novice interpreter may quickly recognize faults and channels on attribute time slices, karst terrains provide more complex patterns. We sought to instruct the attribute expression of a karst terrain in the western part of the Fort Worth Basin, Texas, United States of America. Karst provides a specific expression on almost every attribute. Specifically, karst in the Fort Worth Basin Ellenburger Group exhibits strong dip, negative curvature, low coherence, and a shift to lower frequencies. Geomorphologically, the inferred karst geometries seen in our study areas indicate strong structural control, whereby large-scale karst collapse is associated with faults and where karst lineaments are aligned perpendicularly to faults associated with reflector rotation anomalies.

## Introduction

The word *karst* is a German word that denotes the area of modern Slovenia known as Kras and known to the ancient Romans as Carso. The well-drained limestone terrain and extensive system of natural caverns make Kras an important wine-producing area. The word *karst* is now used to describe a carbonate terrain that has undergone significant diagenetic alteration, which gives rise to enhanced joints, caves, and collapse features. Paleokarst plays many roles in oil and gas reservoirs. The Ordovician paleokarst is a main oil and gas reservoir in the Tarim Basin, China, in which the reservoir depth can reach 6–7 km (Chen et al., 2010). Across the Central Basin Platform of West Texas, karst processes are responsible for the vuggy reservoir rock, and also the anhydrite-plugged updip seal (Duo et al., 2011). In shale resource plays, such as the Barnett Shale unconformably lying upon the Ellenburger in many areas of the Fort Worth Basin, karst can form geohazards. Wells that intersected collapse features and diagenetically altered faults and joints will produce much water from the underlying aquifer, which should be abandoned. In the Barnett and Eagle Ford shale, such hazards are often fault controlled, and many interpreters call this a *string of pearls* (Schuelke, 2011). In the Mississippi lime play of northern Oklahoma and southern Kansas where the average water cut is 95%, the deeper Ordovician-age karst Arbuckle (Ellenburger equivalent) Formation provides the capacity to dispose of the water (Elebiju et al., 2010).

The Fort Worth Basin Texas Barnett Shale was the first successfully exploited shale resource play in North America. Like most resource plays, the low-permeability Barnett Shale serves as the source rock, reservoir rock, trap, and seal. Production is most often achieved through the use of horizontal wells and hydraulic fracturing. In the core producing area of the Fort Worth Basin, the Barnett Shale lies below the Marble Falls Limestone and above the Viola Limestone (Figure 1). In general, quartz- and dolomite-rich rocks are brittle, whereas calcite-rich rocks are ductile (Wang and Gale, 2009). In our study area, the Barnett Shale lies unconformably on top of the relatively brittle, dolomitic Ellenburger Group (Holtz and Kerans, 1992). Here, the extensively karst-modified Ellenburger presents numerous drilling-related risks.

Faults and fractures, associated with Ellenburger collapse, often propagate through the overlying Barnett Shale. Sullivan et al. (2006) and Roth and Thompson (2009) describe fault-controlled collapse features in a

---

[1] University of Oklahoma, ConocoPhillips School of Geology and Geophysics, Norman, Oklahoma, USA. E-mail: kmarfurt@ou.edu; jie.qi@ou.edu; bo.zhang-1@ou.edu; zhouhuailai06@cdut.cn.

Manuscript received by the Editor 1 December 2013; revised manuscript received 8 May 2014; published online 4 August 2014. This paper appears in *Interpretation*, Vol. 2, No. 3 (August 2014); p. SF91–SF110, 22 FIGS.

http://dx.doi.org/10.1190/INT-2013-0188.1.

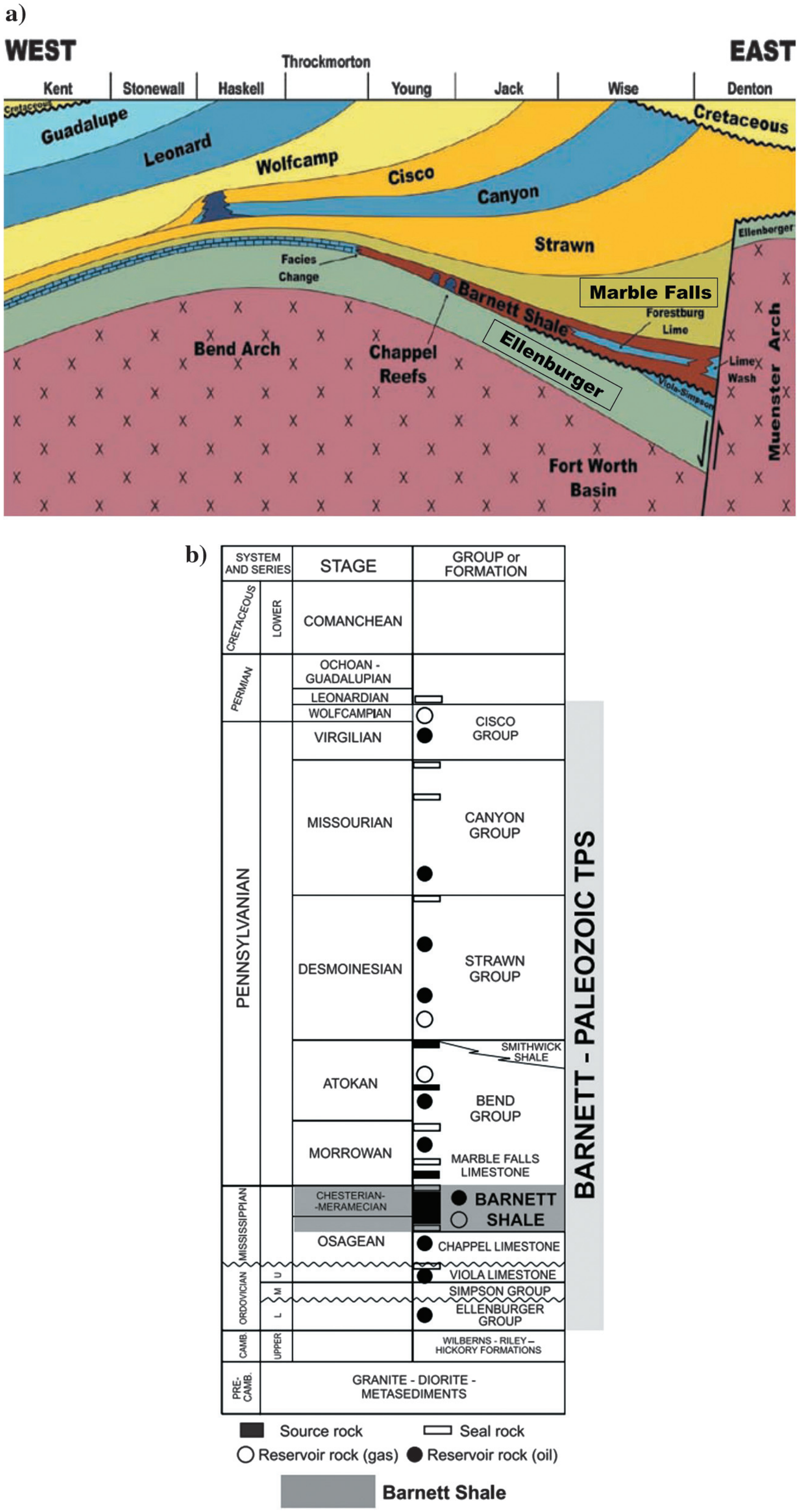

**Figure 1.** (a) Stratigraphic cross section and (b) stratigraphic column of the Fort Worth Basin. In the core study area of Wise and Denton Counties to the east, the Barnett Shale is subdivided into upper and lower units by the intervening Forestburg Lime. The calcite-rich geomechanical ductile Marble Falls and Viola Limestones from hydraulic fracture barriers. The Viola fracture barrier pinches out to the west, such that the Barnett Shale lies unconformably on top of the more brittle, dolomitic Ellenburger Group. The survey in the following figures is on strike with the area of Young County in this image (after Pollastro et al., 2007).

survey without a Viola hydraulic fracture barrier in western Wise County, Texas (Figure 1). Khatiwada et al. (2013) describe basement control of karst using the same survey described in this paper. Hardage et al. (1996) and McDonnell et al. (2007) describe how these deeper collapse features locally enhanced accommodation and provided depocenters for Pennsylvanian-age Bend Conglomerates.

Seismic attributes are routinely used to map geologic features of interest. Coherence (e.g., Bahorich and Farmer, 1995) is routinely used to identify faults and channel edges. Curvature (e.g., al-Dossary and Marfurt, 2006) is used to map folds and flexures. Spectral components (e.g., Partyka et al., 1999) are used to constrain lateral variations in channel thickness. Qi and Castagna (2013) illuminate faults and karst detection using amplitude and phase spectrum and PCA fault-detection attribute, which calculates the first principal component of the most-positive curvature, coherence, variance, and phase spectrum. Often, interpreters want to know which attribute is best for illuminating a particular geologic feature. In this tutorial, we illustrate the value of using multiple seismic attri butes to illuminate paleokarst terrain features common within the Fort Worth Basin. We will argue that the integrative use of mathematically independent attributes can reduce the risk of interpreter error.

We begin our tutorial with a brief summary of the geology of the study area. Next, we describe poststack data conditioning that suppresses migration artifacts and improves spectral bandwidth. Then, we introduce a suite of seismic attributes, first, displaying them as time slices through attribute volumes, then as horizon slices along the upper Ellenburger. As we discuss each attribute, we attempt to link the attribute expression to a specific component of the geology (e.g., the structural dip of collapse features). We will also address potential interpretation pitfalls when mathematically coupling attributes. We conclude by providing insights into the geology of the Fort Worth Basin and showing the value of multiattribute visualization. The details of algorithm descriptions can be found in Appendix A.

## Geologic background

The Fort Worth Basin is one of several basins that formed during the late Paleozoic Ouachita Orogeny, generated by convergence of Laurasia and Gondwana (Bruner and Smosna, 2011). The Mississippian-age organic-rich Barnett Shale gas reservoir is a major resource play in the Fort Worth Basin. It extends more than 28,000 $\text{mi}^2$ with most production coming from a limited area, in which the shale is relatively thick and isolated between effective hydraulic fracture barriers. Conformably overlying the Barnett Shale is the Marble Falls Formation. The lower Marble Falls consists of a lower member of interbedded dark limestone and gray-black shale. Underlying the Barnett Shale are the Ordovician Viola-Simpson Formations, which dominantly consist of dense limestone, and dolomitic Lower Ordovician Ellenburger Group.

The upper surface of the Ellenburger records the second-order Sauk-Tippecanoe erosional unconformity, which is characterized by extensive karst and solution collapse (Loucks, 2003). Lucia (1971) first recognized the genetic relationship between karst dissolution and breccias seen in the Ellenburger Group. Kerans (1989, 1990) establishes the karst and cave models (Figure 2) and their development in the Ellenburger Group. This paleocave model forms the basis of the paleokarst model, which includes a paleocave floor, fill, and roof. Faulting and local subsidence may also be associated with karst and solution-collapse features on the top of the Ellenburger Group (Gale et al., 2007). Pore networks in the Ellenburger Group are complex because of the amount of brecciation and fracturing associated with karst. In the Fort Worth Basin, the Ellenburger Group is almost always a water-bearing formation. Faults and karst in the Ellenburger Group provide vertical conduits into the overlying Barnett Shale. Hydraulic fracturing may open these zones of weakness resulting in a well that produces large quantities of water. For this reason, mapping karst, joints, and fault geohazards in the Ellenburger Group is an important precursor to successful Barnett Shale completion.

Karst-related fractures are common in the upper Ellenburger (Kerans, 1989). Tectonic faults can serve as conduits for meteoric fluids that water circulation, which favor subsequent dissolution (Loucks, 2008). Preferential dissolution along intersecting joints and faults give rise to elliptical collapse features (Sullivan et al., 2006). Although karst is usually associated with meteoric waters, bottoms-up karst (i.e., hydrothermal alteration) can also occur (Sullivan et al., 2003). Operators have found copper mineralization in at least one Wise County well. Mineralization of Mississippi lime fractures are common in Osage County, Oklahoma, and commercially exploitable Mississippi Valley type lead-zinc deposits occur further east in the tristate area of Oklahoma, Kansas, and Missouri (Leach et al., 1993). Elebiju et al. (2010), Sullivan et al. (2006), and Khatiwada et al. (2013) provide evidence of basement-controlled faulting, hydrothermal mineralization, and collapse chimneys in the Fort Worth Basin. We expect similar mineralization and bottoms-up karst within our study area.

## Data conditioning

A 3D seismic acquisition program was undertaken in 2006 by Marathon Oil Company using 16 live receiver lines forming a wide-azimuth survey with a nominal 16 × 16 m (55 × 55 ft) CDP bin size to image the Barnett Shale at approximately 914 m (3000 ft) true vertical depth subsea (TVDSS) or 0.7 s two-way time (TWT) (Roende et al., 2008). Although data quality is excellent, minor improvements through poststack data conditioning can significantly facilitate and improve subsequent interpretation. Our poststack data-conditioning workflow is shown in Figure 3a. This workflow contains two major steps: The first step is application of principal-component structure-oriented filtering (SOF) and the second step is spectral balancing. Figure 3b indicates general steps of principal-component SOF. We can create a single waveform, which best fits with each original seismic trace (steps 1 and 2, Figure 3b). The waveform is the best coherent wavelet that fixes each trace by the approximate scale, which calculates from the best-fit waveform and each trace. The lateral variation of the amplitude along the structural dip is called the eigenmap $v^{(1)}$. One can take derivatives of this eigenmap. Such derivatives will be the input for subsequent calculations of amplitude curvature. Figure 4 shows the spectrum for the entire survey before (a) and after (b) and a representative seismic line before (c) and after (d) the data-conditioning workflow. A common spectral balancing approach is to estimate the coherent (signal) part of the seismic trace as that which crosscorrelates with neighboring traces. We estimate the coherent part of the seismic trace using two

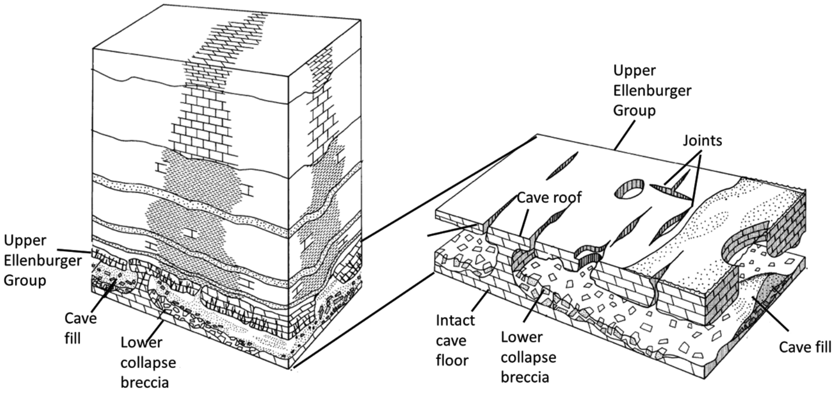

**Figure 2.** Genetic paleocave model for the Lower Ordovician of West Texas showing cave floor, cave roof, and collapsed breccia (modified after Kerans, 1988, 1989).

passes of a nine-trace structure-oriented filter. To minimize the risk of impact of removing geology, we then apply a single time-variant spectral balancing operator to the entire volume. Note that low-amplitude (but annoying) crosscutting migration noise is suppressed, and fault and karst edges are preserved. This data-conditioning routing focuses on improving the resolution in the thin Barnett Shale and the Ellenburger Group.

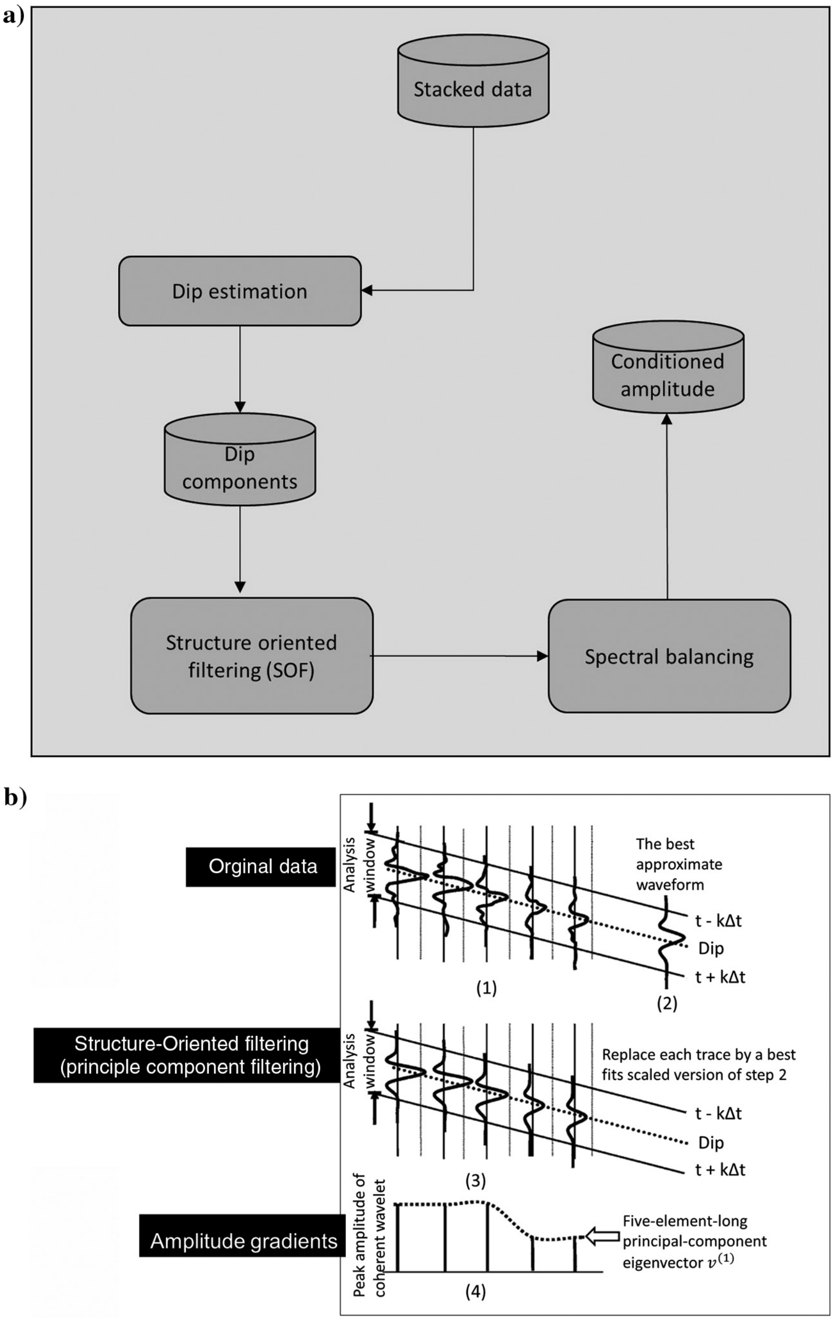

**Figure 3.** Workflow (a) to precondition the seismic data prior to attribute computation and (b) illustrating the steps for SOF based on principal component analysis (modified after Marfurt, 2006). The filtered seismic amplitude is then spectrally balanced using the average time-frequency distribution computed using a matching-pursuit spectral decomposition algorithm described by Liu and Marfurt (2007).

## Karst on attribute time slices

### *Seismic amplitude*

Seismic amplitude is the most common attribute used in seismic interpretation. If a geologic feature is not measurable by seismic amplitude and phase, no derivative attributes will enable identification. In Figure 4c and 4d, we see two strong reflections representing the top of Marble Falls and the top of Ellenburger. The organic-rich Barnett Shale is located between these two units (Figure 1). Three karst collapse features are recognizable on this section. The largest karst doline is visible along the margins of a fault, and two smaller compaction-induced sags are situated some distance away from any faults. Below the top of the collapses, within the Ellenburger, and below collapse features, rapid changes in reflector dip, a decrease in continuity, and a decrease in frequency are seen. Figure 5 shows a time slice at $t = 0.750$ s through the seismic amplitude volume. Red arrows indicate faults that are better delineated by attribute processing. However, note that the larger karst doline features indicated by the yellow arrows are clearly seen within the traditional amplitude volume. This appearance is our first example of mixed attribute response. That is, the elliptical features are not a function of lateral changes, but rather lateral change in reflection time, or dip, resulting in the onion ring. The green arrow marks a smaller karst features that is to be seen in seismic amplitude slices.

### *Structural dip*

A major characteristic of karst collapse is their bowl-shape appearance with strongly dipping sides. Figure 6 shows time slices at $t = 0.750$ s for apparent dip components at 0°, 45°, 90°, and 135° from north. Figure 7 shows the mathematical model in defining reflector dip. Figure 8a shows their corresponding dip magnitude, and Figure 8b illustrates the dip azimuth modulated by dip magnitude using a 2D color bar. The larger karst collapses (yellow arrows), and the major faults (red arrows) exhibit high-dip anomalies. Very subtle flexures and joints are best illuminated by the apparent dip component perpendicular to them. As observed in Figure 6, large bowl-shaped karst collapse features are coincident with large faults with laterally extensive damage zones. The red dashed lines in Figure 8a and 8b suggest that these large karst collapse features are structurally linked by faults or joints, giving rise to what many interpreters refer to as a *string of pearls* (Schuelke, 2011). We interpret the features indicated by the blue arrows to be eroded valleys or cave collapses described in Kerans (1988, 1989, 1990) paleocave models. Other low-magnitude anomalies (green arrows) are likely smaller scale karst features that are relatively distal to the major fault zones. Orange arrows indicate a relatively rugose surface that is free of large collapse. These rugose areas fall below the interface between the top Ellenburger and the lower Barnett Shale.

Correlating the dip-magnitude, dip-azimuth attribute time slices (Figure 8) to the apparent dip components (Figure 6), reveals collapse features that are expressed as steeply dipping edges which in this image appear as black ellipses. Although the components of vector dip are useful for interpretation, they also serve as input for other attributes. Reflector curvature, rotation, and convergence are directly computed from vector dip, whereas coherence, amplitude gradients, textures,

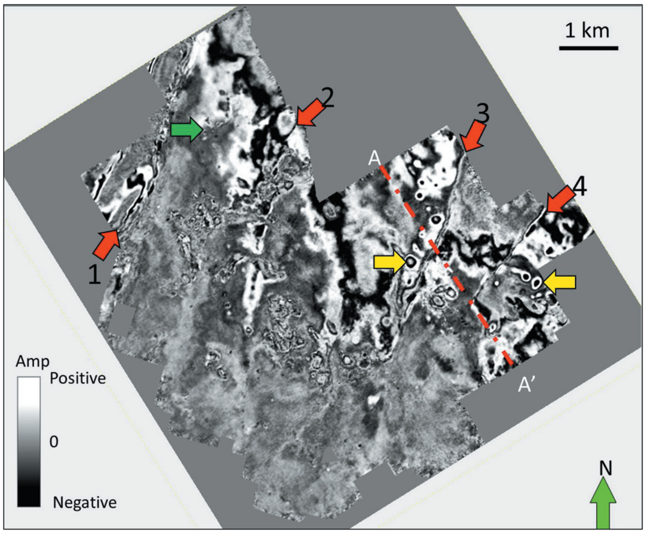

**Figure 5.** Time slice at $t = 0.750$ s through the seismic amplitude volume at the approximate top Ellenburger horizon. Faults are indicated by red arrows. Large karst appear as circular features (yellow arrows). Smaller karst (green arrow) are less obvious but can also be seen. The location of line AA′ shown in the previous image is indicated by the red dashed line.

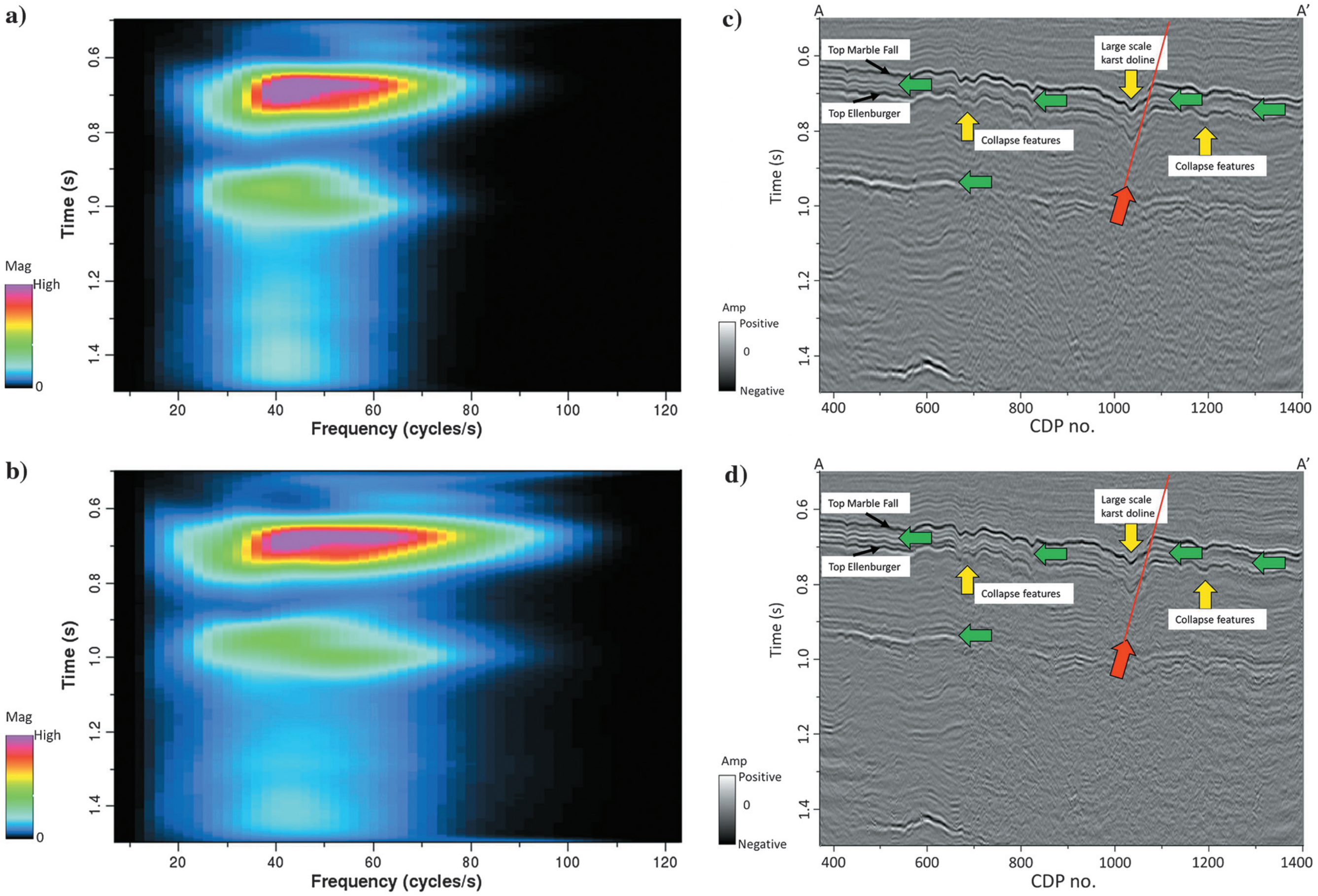

**Figure 4.** Average time-frequency spectrum for the entire survey (a) before and (b) after spectral balancing using a bluing factor of $f^{\beta}$, where $\beta = 0.3$. Note the increase in frequency content between $t = 0.6$ and $t = 0.8$ s. Line AA′ (c) before and (d) after time-variant spectral balancing. Note the increase in frequency content within the target Barnett Shale interval between $t = 0.6$ and $t = 0.8$ s as well as the interval above the top basement (green arrows). The red arrow indicates one normal fault, and yellow arrows indicate large-scale karst dolines and collapse features.

and structure-oriented filtering (SOF) are computed along vector dip.

When reflectors are horizontal, displays of azimuth calculations are meaningless. To overcome this limitation, we modulate dip azimuth by dip magnitude using a 2D color bar as shown in Figure 8b. Here, the broad magenta (northeast) and green (southwest) bands indicate rotation about the major normal faults cutting the survey. The dissolutional caves are "brighter" with a radial pattern mimicking the 2D color bar indicating the reflections are dipping into the collapse features.

Additionally, although these faults (numbers 1–4) exhibit a similar orientation, they are of different scales in dip magnitude (Figure 8a), and they are of different anomalies in apparent dip (Figure 6) and dip azimuth (Figure 8b). Fault (no. 4) has opposite hanging wall and footwall position (this difference can be seen on the time-structure map). We interpret these faults to have been caused by the same normal geologic stress,

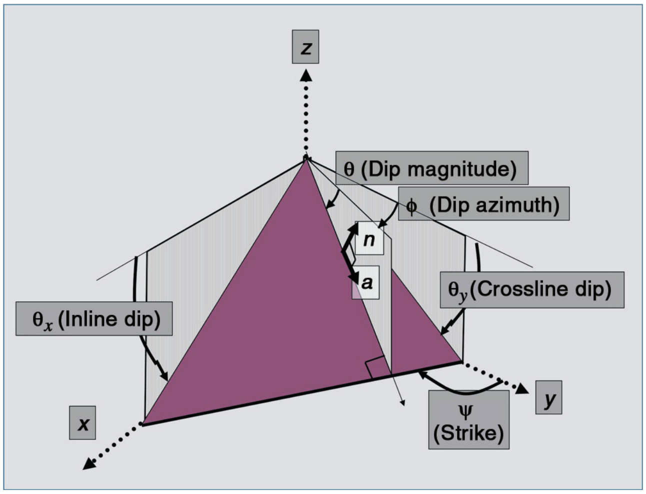

**Figure 7.** Mathematical model in defining reflector dip (modified after Marfurt, 2006). By convention, $n$ = unit vector normal to the reflector; $a$ = unit vector dip along the reflector; $\theta$ = dip magnitude; $\phi$ = dip azimuth; $\psi$ = strike; $\theta_x$ = the apparent dip in the $xz$- plane; and $\theta_y$ = the apparent dip in the $yz$- plane.

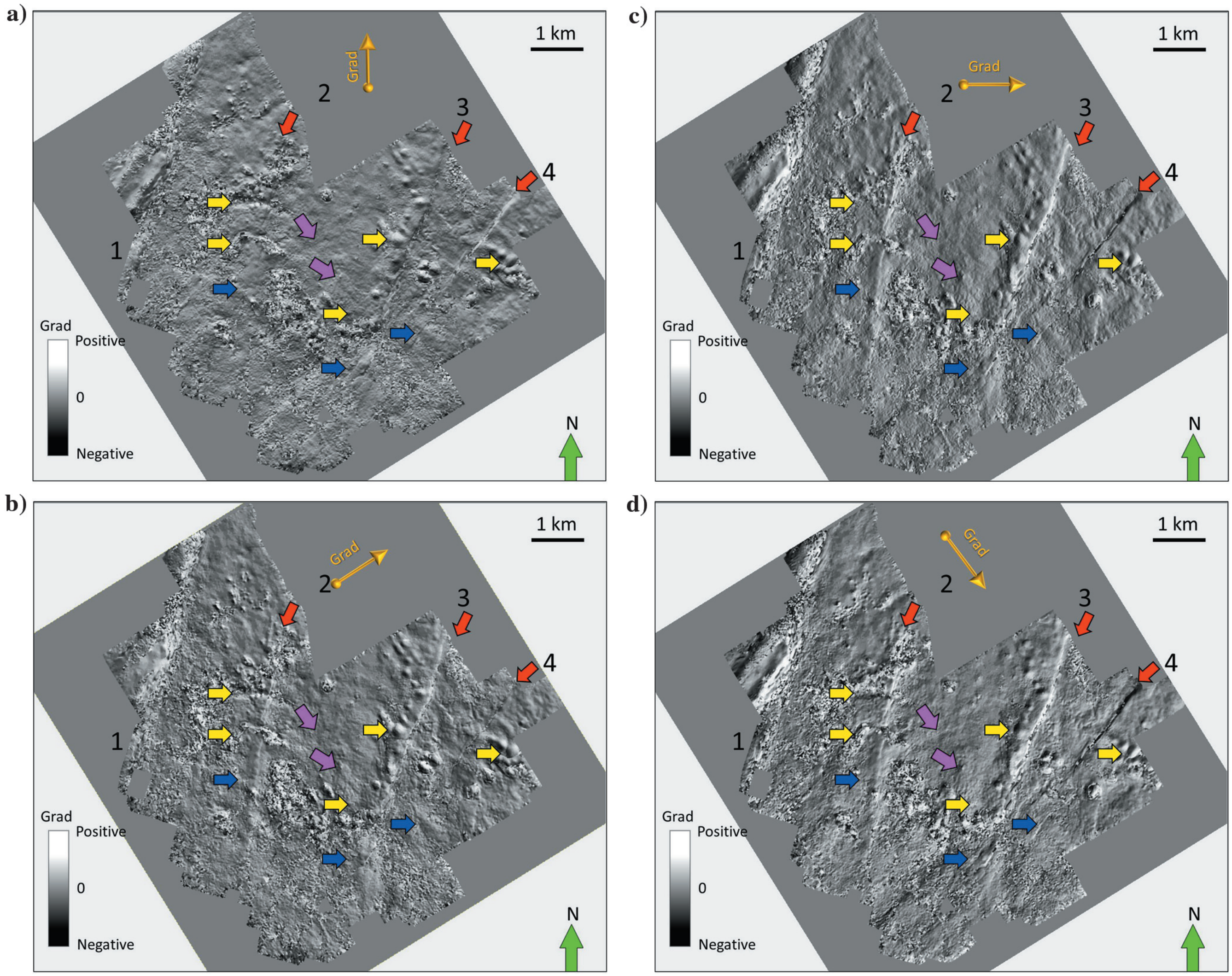

**Figure 6.** Time slices at $t = 0.75$ s through apparent dip volumes at (a) 0°, (b) 45°, (c) 90°, and (d) 135° from the north. Yellow arrows indicate channels or cave collapse. Red arrows indicate major faults, pink arrows indicate minor flexures, and blue arrows indicate joints.

but perhaps cutting different lithologies, giving rise to different patterns on the left and right areas of the time slice.

We zoom in on two zones of interest seen on the dip magnitude time slice in Figure 9a and display them in Figure 9b and 9e. We then draw two profiles that cut the collapse and fault features of interest and display line BB′ in Figure 9c and line CC′ in Figure 9d. Line BB′ (Figure 9c) crosses a major fault (red arrow), two large-scale karst collapse features (yellow arrow) and a channel-like collapse feature (blue arrow). Line CC′ (Figure 9d) crosses three large-scale karst collapse features and a major fault. The karst and channel-like collapse features exhibit synclinal cross sections at the Top Marble Falls and the Top Ellenburger. Light green arrows indicate a bright spot anomaly under the largest karst collapse feature, which we interpret to be due to infill with lower impedance, perhaps fractured or brecciated material. Green arrows in Figure 9e indicate small-scale karst collapse features, which exhibit less bright basal reflections in Figure 9g. Not all karst collapse features exhibit bright bottom reflections, suggesting heterogeneity in their fill.

### *Coherence*

Karst not only gives rise to changes in reflector dip and azimuth, but also to changes in the seismic waveform continuity. We use vector dip as input for principal-component SOF in the most coherent window, which represent lateral amplitude variation, to constrain random and coherent noise and improve vertical resolution (Marfurt, 2006). Figure 10 shows a time slice through a coherence volume computed by taking the ratio of the energy of a principal-component (structural-oriented) filtered data based on the workflow shown on Figure 3b to the energy of the original data. Comparing this image with the previous image of reflector dip we note that the faults (red arrows) and large collapse features (yellow arrows) do appear somewhat weaker. Because coherence is computed along structural dip, this implies that there is a small offset ($<1/4\lambda$) and only small changes in waveform across the edges of the collapse. Low coherence and high dip magnitude at yellow arrows indicates that this incised valley has little offset along its flanks. When examining vertical slices time through the amplitude data (Figure 4c and 4d), note that the dissolution within the Ellenburger is significantly less at $t = 0.7$ s at the Barnett Shale level, with the shale layers draped over the collapse feature. Similarly, the blue arrows indicates karst valleys, which are not as well defined as those observed in the dip magnitude volume. We conclude that these large collapse features are coherent in lateral amplitude or waveform; however, their laterally variable dip is not imaged using coherence. Orange arrows indicate incoherent, rugose eroded surfaces that are free of large collapse features, which suggests lithology changes from southwest to northeast. These incoherent surfaces do not appear to be fault controlled. Green arrows indicate small karst features.

### *Spectral decomposition*

Lateral changes in layer thickness and impedance produce lateral variation in spectral components. Karst-related diagenetic products generate lateral changes in porosity, and from limestone to dolomite (Lucia, 1995). In our study area, dissolution collapse features within the underlying Ellenburger Group generate small faults ($<1/4\lambda$) and fractures in the overlying Barnett Shale, reducing velocity and acoustic impedance and in turn resulting in lateral changes in tuning thickness. Chaotic collapse features and rugose surfaces give rise to nonspecular scattering, with constructive interference at low frequencies and destructive interference and at high frequencies, thereby shifting the spectra lower.

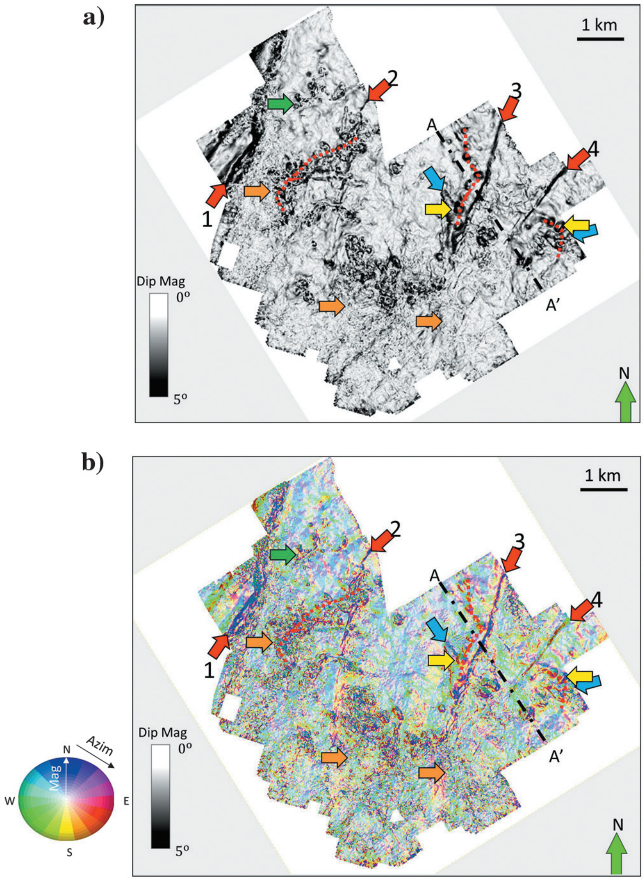

**Figure 8.** Time slice at $t = 0.750$ s through (a) volumetric dip and (b) the dip azimuth modulated by dip magnitude using a 2D color bar. Red arrows indicate faults that control many of the larger collapse features. Dashed red lines show a string-of-pearls feature, which, when correlated with the most-negative curvature, indicates control by diagenetically altered joints or faults with little vertical offset. We interpret the feature indicated by the blue arrows to be a valley or cave collapse, or channel-like collapse features. The green arrow indicates small-scale karst that are far from major fault zones. Orange arrows indicate a relatively rugose surfaces that are free of large collapse features.

Figure 11a shows a time slice at $t = 0.750$ s through the peak spectral magnitude volumes computed using a matching pursuit algorithm described by Liu and Marfurt (2007). Note the improved resolution of the peak spectral magnitude in illuminating the dissolutional cave edges and internal discontinuities. Blue arrows indicate suspected paleovalleys or collapsed paleocaverns that reveal low spectral magnitude. Orange arrows indicate large karst features, which were identifiable using previously described coherence image (Figure 10).

Peak frequency and peak phase are meaningful if the corresponding magnitude is above the noise level. If so, we suggest using magnitude to modulate these images (Figure 11b). Note the shift to low values of peak frequency (magenta to red) above collapse features, which represents the destructive interference at the higher frequencies. The high frequencies (cyan to blue) record thinner layers in the Barnett Shale (low magnitude). In Figure 11b, the orange arrows point to low-frequency features that correspond to rugose surfaces as shown in the coherence attributes (Figure 10) and peak mag-

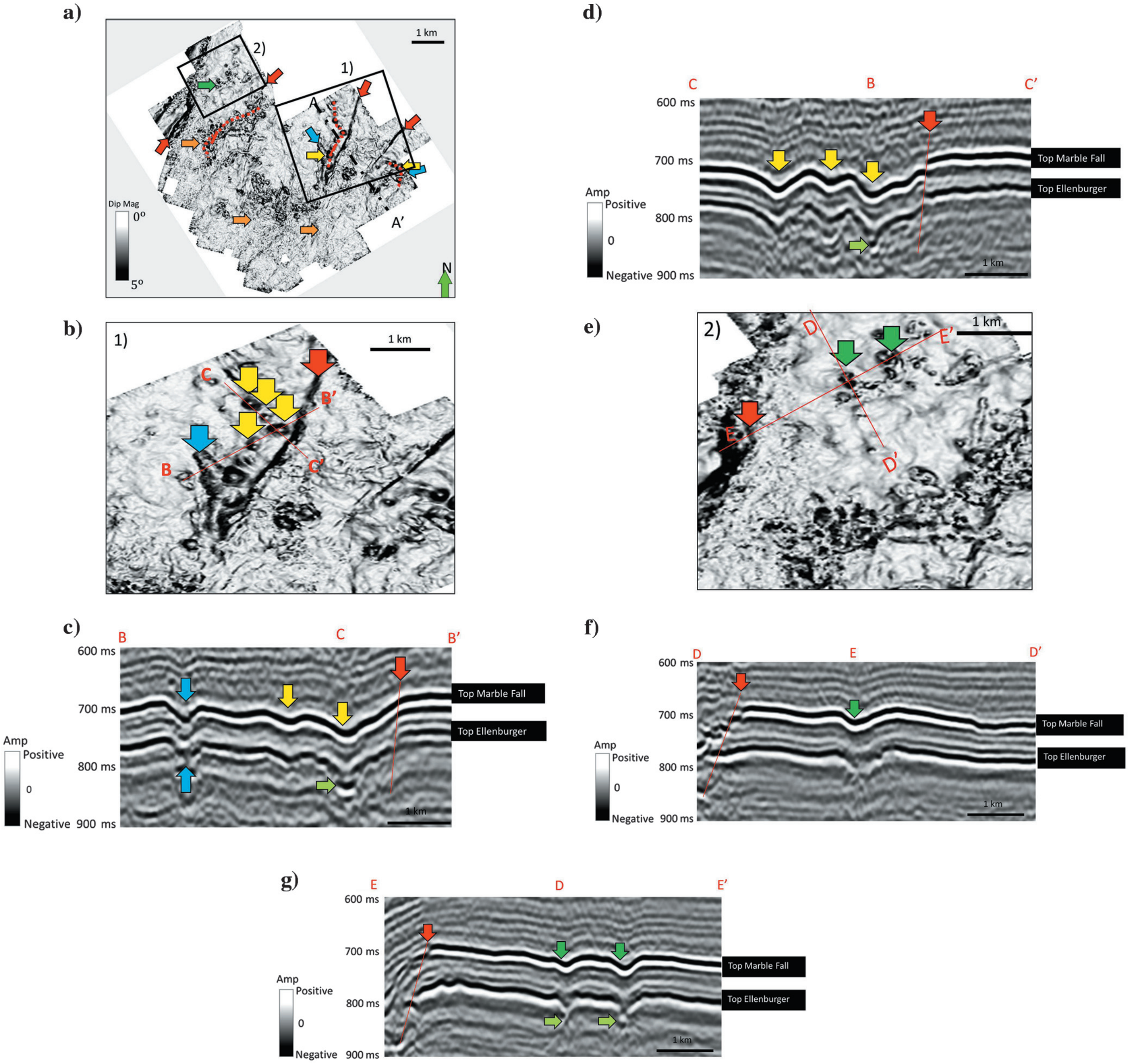

**Figure 9.** Time slice at $t = 0.750$ s through (a) volumetric dip, and (b and e) zoomed in zones. (c, d, f, and g) are seismic section view of lines BB′, CC′, DD′, and EE′ show large-scale karst collapse features (yellow arrows), major faults (red arrows), channel-like collapse features (blue arrows), and small-scale karst collapse features. Notice that not all karst collapse features exhibit bright bottom reflections, suggesting heterogeneity in their fill.

nitude attributes (Figure 11a). Given the rugose nature of this surface, time slices through the peak phase spectrum provide only limited interpretational value.

### *Structural curvature, reflector rotation, and reflector convergence*

Structural curvature is computed by taking the derivatives of the dip components as shown in Figure 6. As such, we expect curvature to highlight joints and fractures characterized by more subtle, longer wavelength joints and flexures. Reflections that exhibit similar waveforms, that is, those having small offset ($<1/4\lambda$) and subtle changes in dip across faults, will generate curvature, but not coherence anomalies (Al-Dossary and Marfurt, 2006). The amplitude of the curvature anomaly is inversely proportional to the radius of curvature at each voxel, with negative values indicating synclinal, and positive values anticlinal deformation (Figure 12).

Figure 13a and 13b contrasts the most-positive and most-negative structural curvature along the same time slice. In this survey, the major faults are expressed by a positive curvature anomaly across the footwall, which

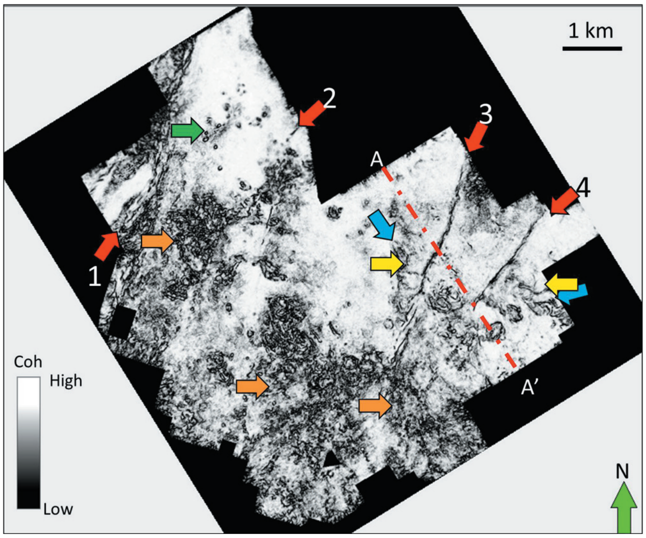

**Figure 10.** Time slice at $t = 0.750$ s through eigenstructure-based coherence. Note that the faults (red arrows), channel-like collapse features (blue arrows), and large collapse features (yellow arrows) do not appear as strong as in the dip magnitude image. Orange arrows indicate incoherent, rugose surfaces that are free of large collapse features.

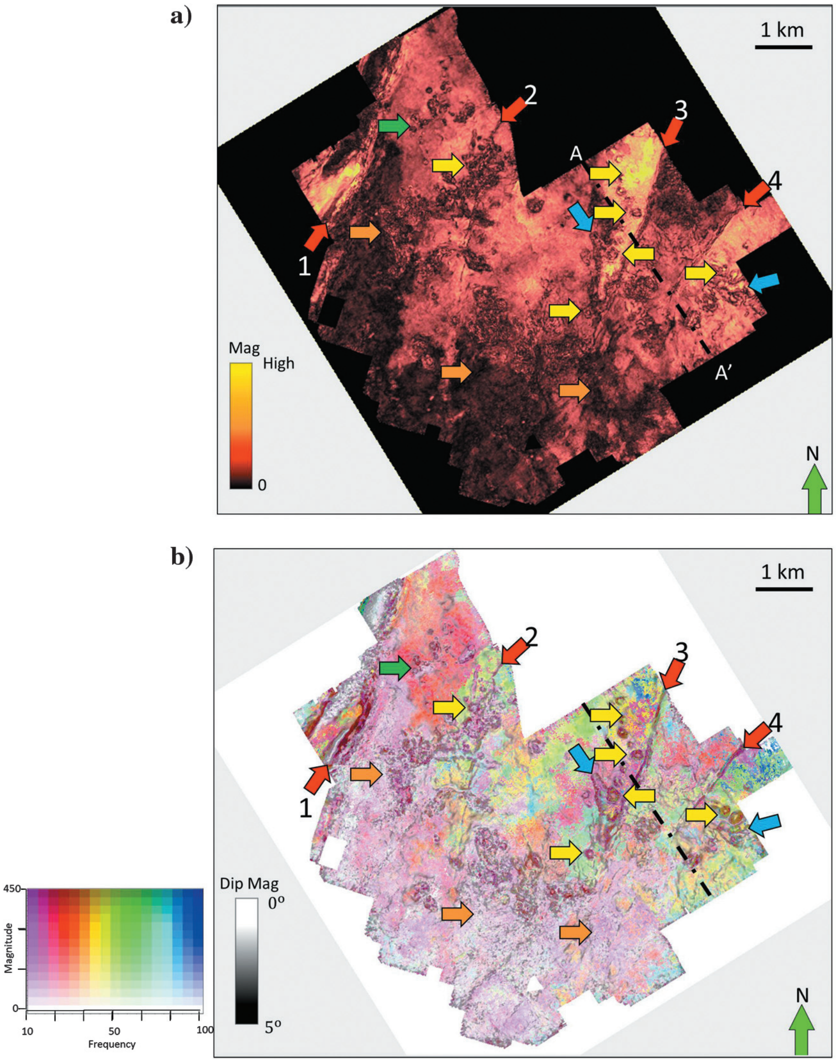

**Figure 11.** Time slice at $t = 0.750$ s through (a) the peak spectral magnitude volumes computed using a matching pursuit algorithm described by Liu and Marfurt (2007) and (b) peak magnitude and frequency modulated images corendered with dip magnitude image. Yellow arrows indicate large-scale karst features. Red arrows indicate faults, blue arrows channel-like collapse, and green arrows indicate small karst shown in the previous image. Orange arrows indicate a relatively rugose surfaces that are free of large collapse features.

is laterally offset from a corresponding negative curvature anomaly across the hanging wall. This curved appearance is commonly observed in 3D seismic volumes of carbonate terrains associated with conjugate faults, which are below seismic resolution and are morphologically similar to those described by Ferrill and Morris (2008). The dip magnitude and coherence anomalies fall between the two curvature anomalies. In this image (Figure 13), the bowl-shaped collapse features express a negative value and appear as blue ellipses (yellow and green arrows). The rugose surface (orange arrows) is a product of a shorter wavelength and indicates less deformation. Yellow polygons enclose an area, in which large collapse features are coincident with high-angle normal faults. The dissolution caves zone is coincident with through-going faults terminate in the Marble Falls formation. The fault damage zone consist of fractures and small-scale faults shown as small red lines on the most-positive curvature and blue channels crossed between faults and karst. To visualize the relation between karst and faults, we corender most-positive and most-negative curvature with dip magnitude (Figure 13c and 13d). The dip-magnitude attribute accurately maps the location of faults and karst boundary, while the shape of karst features and more-subtle faults is confidently mapped using curvature attributes. When examining Figure 13c and 13d, note that the large karst features appear fault controlled and are cut by smaller faults or joints. These smaller scale features may record compaction-induced fracturing across paleocavern roofs similar to that described by Kerans (1989, 1990). Additionally, reflector rotation and convergence computed from the curvature dip components (Marfurt and Rich, 2010). Reflector rotation (Figure 14a) shows a strong northwest–southeast succession of lineaments, which are strongly aligned and almost perpendicular to northeast–southwest trending faults. Corendering the reflector rotation with dip azimuth as shown in Figure 14a reveals a strong correlation between rotation and inferred karst anomalies. We cannot say without further analysis and outcrop analogues whether this “rotation” is a cause or an effect of the karst features. Interpretations based solely on reflector-vector convergence attributes provides ambiguous results. However, when corendered with dip magnitude (Figure 14b), we recognize that strongly convergent areas correspond to areas characterized by a greater density of faults and karst features. The varying strike of the faults and the elliptical nature of the karst give rise to a complex but easy-to-interpret image.

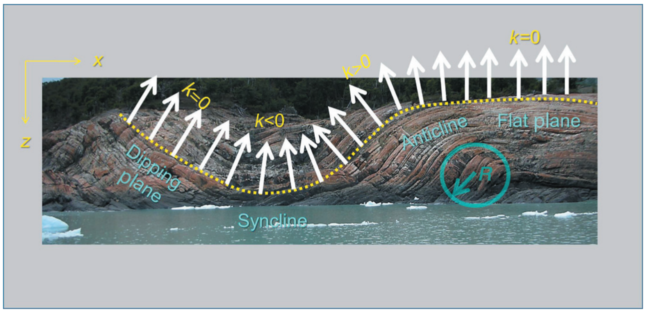

**Figure 12.** Curvature model shows curvature value change based on the plane angle (modified after Marfurt and Rich, 2010).

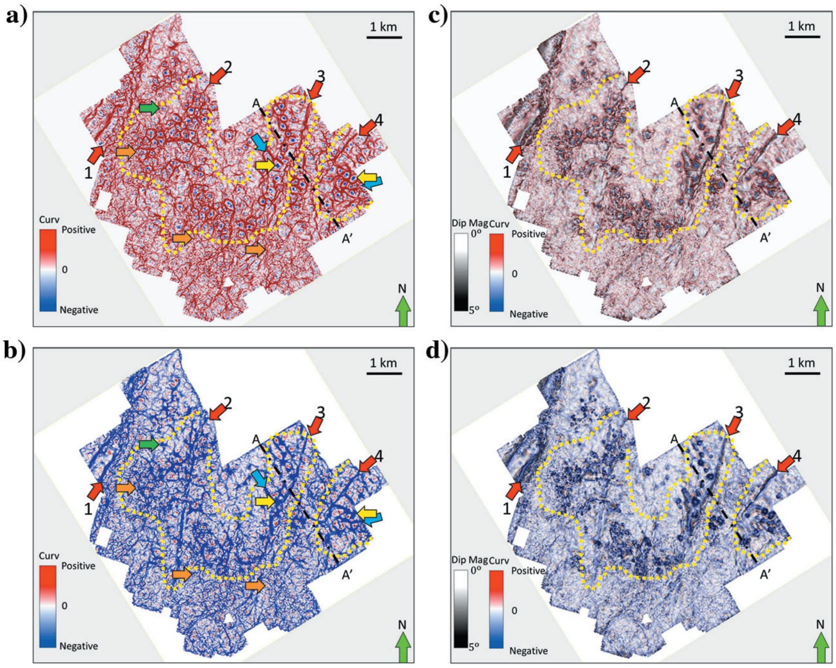

**Figure 13.** Time slice at $t = 0.750$ s through the (a) most-positive and (b) most-negative structural curvature and the (c) most-positive and (d) most-negative structural curvature corendered with dip magnitude. In this survey, the major faults are expressed by a positive curvature anomaly on the footwall which laterally offset from a corresponding a negative curvature anomaly on the hanging wall. The dip magnitude and coherence anomalies fall between the two curvature anomalies. In this image, the bowl-shaped collapse features express a negative value and appear as blue ellipses (yellow and green arrows). The rugose surface (orange arrows) is represented by a shorter wavelength, lower deformation pattern. Yellow polygons indicate the areas where large collapse features are controlled by faults. Blue arrows indicate channel-like collapse features as red anomalies.

### *Amplitude gradients*

If we use a lateral 3 × 3 trace by $n$ sample analysis window, a principal-component (structure-oriented) filter produces a lateral pattern (or 3 × 3 eigenmap) that best represents the lateral variation seen in each of the $n$ vertical amplitude slices. Such filters were used in the SOF described in Figures 3 and 4. Figure 15 is the coherent energy attribute, which is the energy of the filtered data. Computing the energy with an analysis window (±10 ms), we show in Figure 16 the gradient of coherent energy at 0°, 45°, 90°, and 135°. These amplitude gradients are the derivatives of the eigenmap, weighted by its energy. Coherent energy gradient maps can be quite effective for identifying faults and fractures, and can provide constrains for mapping channels, which can be emphasized using lateral changes in tuning (Marfurt, 2006). Like apparent dip, amplitude gradients can be calculated at any azimuth (Figure 6). Overlaying amplitude gradient maps with the coherent energy results in a suite of images that simulates shaded illumination, but of energy, not of time structure. For example, note the shorter wavelength variation of the amplitude gradient images in Figure 16 compared with the structural dip images in Figure 8a. The yellow arrows in Figure 8a indicate high dip anomalies, which are well defined on gradient maps of coherent energy (Figure 16). Lateral variations related to lithologic changes are generally more easily identified on energy than on dip. Large faults and karst are seen in amplitude gradient and structural dip images. Amplitude gradients are computed along the dip, which eliminates dip variability. Such correlation provides independently derived and mutually supportive evidence that the imaged features are likely karst and faults. For Figure 16, green arrows mark small-scale karst and blue arrows indicate channel-like dissolution features; these dissolutions appear as caves and eroded zones on gradient of coherent energy (Figure 16), but they appear as points and discontinuities on coherence (Figure 10).

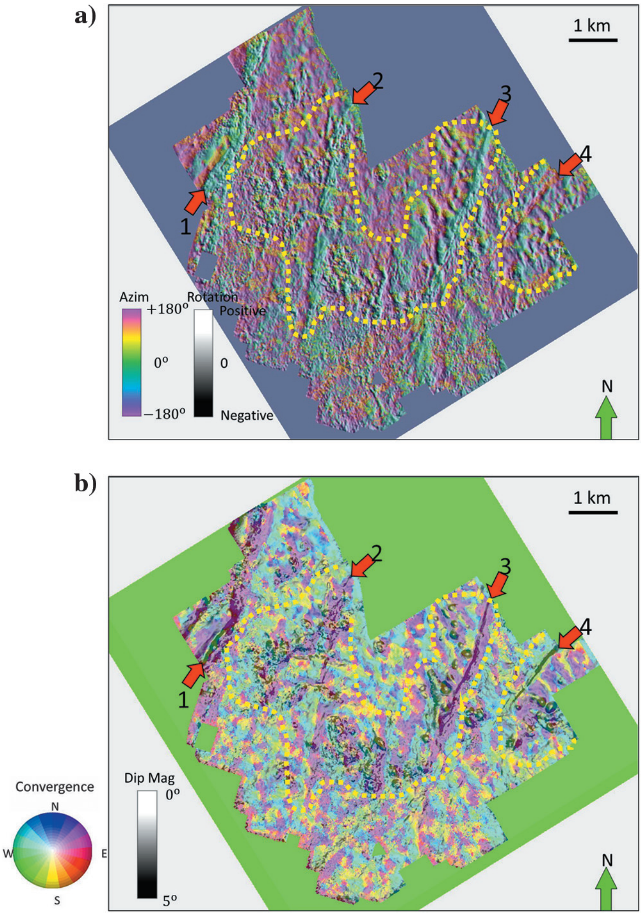

**Figure 14.** Time slice at $t = 0.750$ s through (a) rotation corendered with dip azimuth and (b) vector convergence corendered with dip magnitude. Red arrows indicate major Yellow polygons indicate fault-controlled karst features.

## *Amplitude curvature*

Whereas structural curvature is a derivative of structural dip, amplitude curvature is computed by calculating the derivative of amplitude gradients. Figure 17a and 17b shows the most-positive and most-negative amplitude curvature derived from high-resolution amplitude gradients. With the exception of the dip compensation in the structural curvature computation, the size and the values of both curvature operators are exactly the same. In Figure 17a and 17b, the yellow dashed lines zones indicate complex fault-controlled karst features. Fewer fractures and karst are developed in the areas far away from fault zones. Figure 17c and 17d is the same image way corendered with dip magnitude to highlight karst and better show the relationship among the faults, joints, and karst.

Compared with structural curvature, amplitude curvature delineates several previously overlooked, small circular features in the southern part of the survey where the time slice cuts below the top Ellenburger Dolomite (Figure 18a). Zooming in (Figure 18b), we

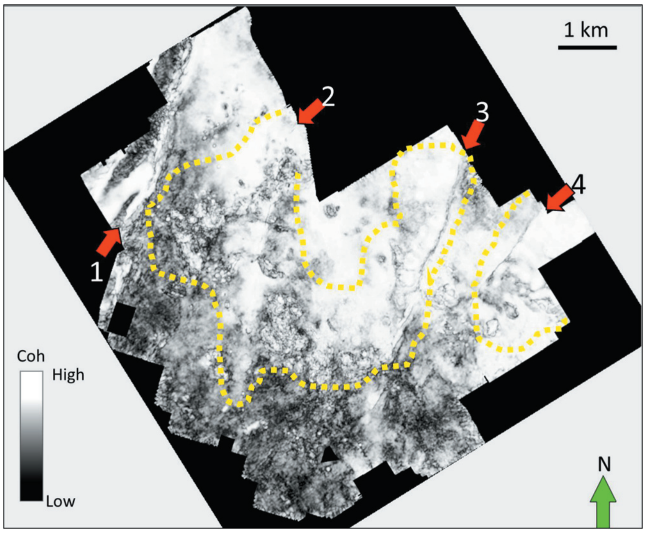

**Figure 15.** Time slice at $t = 0.750$ s through coherent energy attributes. Note that the red arrows indicate major faults, and the yellow polygon indicates fault-controlled karst features.

draw several vertical lines through the seismic amplitude map and display them in the Figure 18c–18f map. The small radius amplitude curvature anomalies appear as bright spot anomalies on the seismic section. Several of them exhibit the string-of-pearls pattern (green arrows in Figure 18c–18e) suggesting they are fault controlled. Those vertical karst anomalies within the Ellenburger have an almost identical appearance to infilled karst collapse features widely seen in the Tarim Basin, China (Chen et al., 2010; Liu et al., 2011; Feng et al., 2012). In the Tarim Basin, the collapse features are filled with Aeolian sands and form excellent oil and gas reservoirs. These subtle karst collapse features within the Ellenburger have a very different morphology from those that cut the Ellenburger and continue into the overlying Barnett Shale and Marble Falls Formations seen in

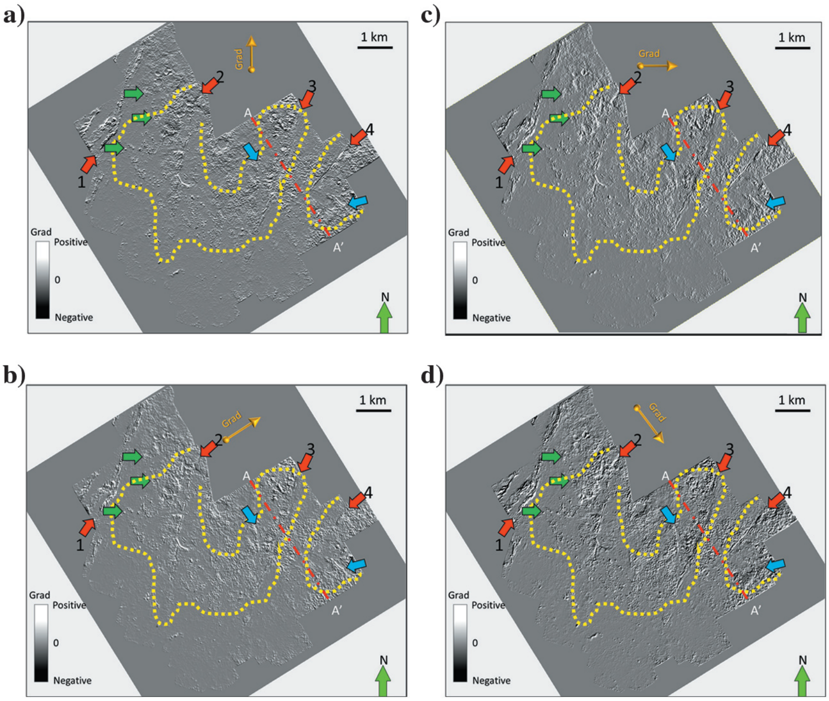

**Figure 16.** Time slices at $t = 0.750$ s through at (a) 0°, (b) 45°, (c) 90°, and (d) 135° from the north amplitude gradients computed along the structural dip. Large karst do not appear to give a strong amplitude anomaly, although small karst (green arrow) do. There does not appear to be a significant acquisition footprint in either of the gradient images. Faults (red arrows) and channel-like collapse features (blue arrows) appear differently on each degree amplitude gradients.

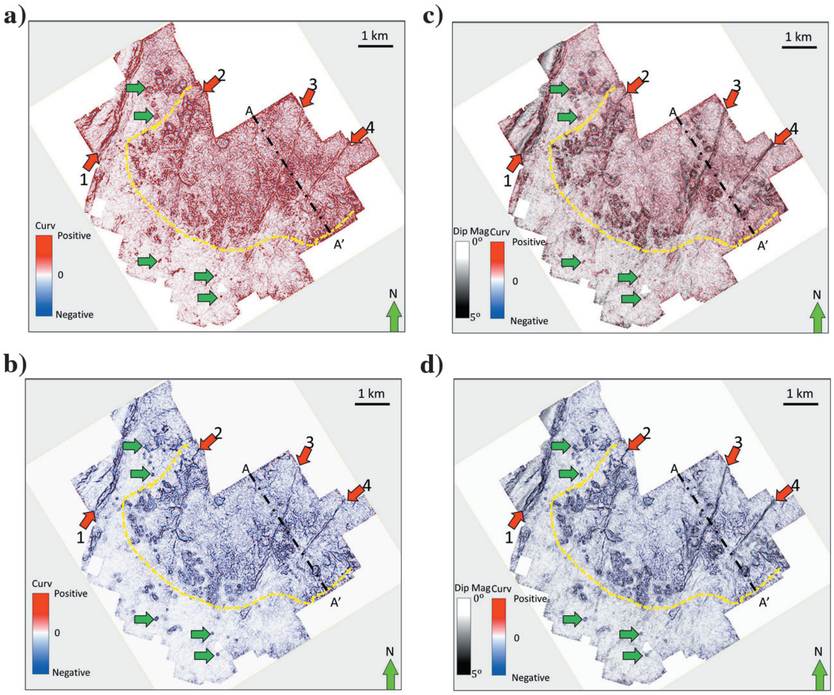

**Figure 17.** Time slices at $t = 0.750$ s through the (a) most-positive and (b) most-negative amplitude curvature and the (c) most-positive and (d) most-negative amplitude curvature volumes corendered with dip magnitude volumes. Dashed yellow polygons indicate areas of fault-controlled karst. Although the structural curvature is computed by taking the derivative of the inline and crossline dip components, the amplitude curvature is computed by taking the derivative of the inline and crossline amplitude gradients shown in the previous image. Yellow dashed line indicates zone dominated by fault-controlled karst. Although northwest–southeast and northeast–southwest lineaments could be the acquisition footprint, we interpret lineaments at other azimuths to indicate diagenetically altered joints giving rise to laterally variable reflectivity. Green arrows indicate the small karst. Some of those can only be highlighted by the amplitude gradient and amplitude curvature.

Figures 9 and 18d. These subtle karst caves appear to be restricted within the Ellenburger and do not significantly alter the base of the Barnett Shale.

Figure 18f shows a subtle collapse-caused fault in seismic section view. The left blue arrow indicates a curved, but continuous feature, whereas the right blue arrow indicates finite displacement along a small fault. Figure 19 shows the subtle faults on different attributes. Notice that dip magnitude, most-positive and most-negative amplitude curvature can detect two kinds of anomalies (blue arrows) at the edges of this subtle collapse-caused faults; however, coherence can only detect the discontinuity associated with the faulted edge.

## Karst on attribute horizon slices

Conventional interpretation is based on mapping faults and horizons. Although faulted horizons are difficult and time consuming to interpret, karst surfaces are particularly tedious for the interpreter because of their discontinuous character and high rugosity. As with any unconformity, autotrackers fail when the overlying strata juxtapose lateral changes in impedance. Interpreting karst topography is exceedingly difficult as the unconformity frequently crosscuts strata with different lithologies characterized by highly variable impedance. Where conventional 3D interpretation fails, incorporation of horizon slices from attribute volumes provide an increasingly valuable alternative method for interpreting complex stratigraphic features, such as karst.

Figure 20 shows the time-structure map at the top Ellenburger Group corendered with a representative vertical slice through the seismic amplitude volume. The structure map shows increased rugosity of the surface toward the south. Figure 21a and 21b shows a horizon slice through the most-positive and most-negative curvature volumes. Dashed yellow lines indicate fault-controlled karst within the Ellenburger Group. Figure 21c and 21d shows the same horizon slices through the curvature corendered with coherence volumes. Black anomalies indicate discontinuities (faults, joints,

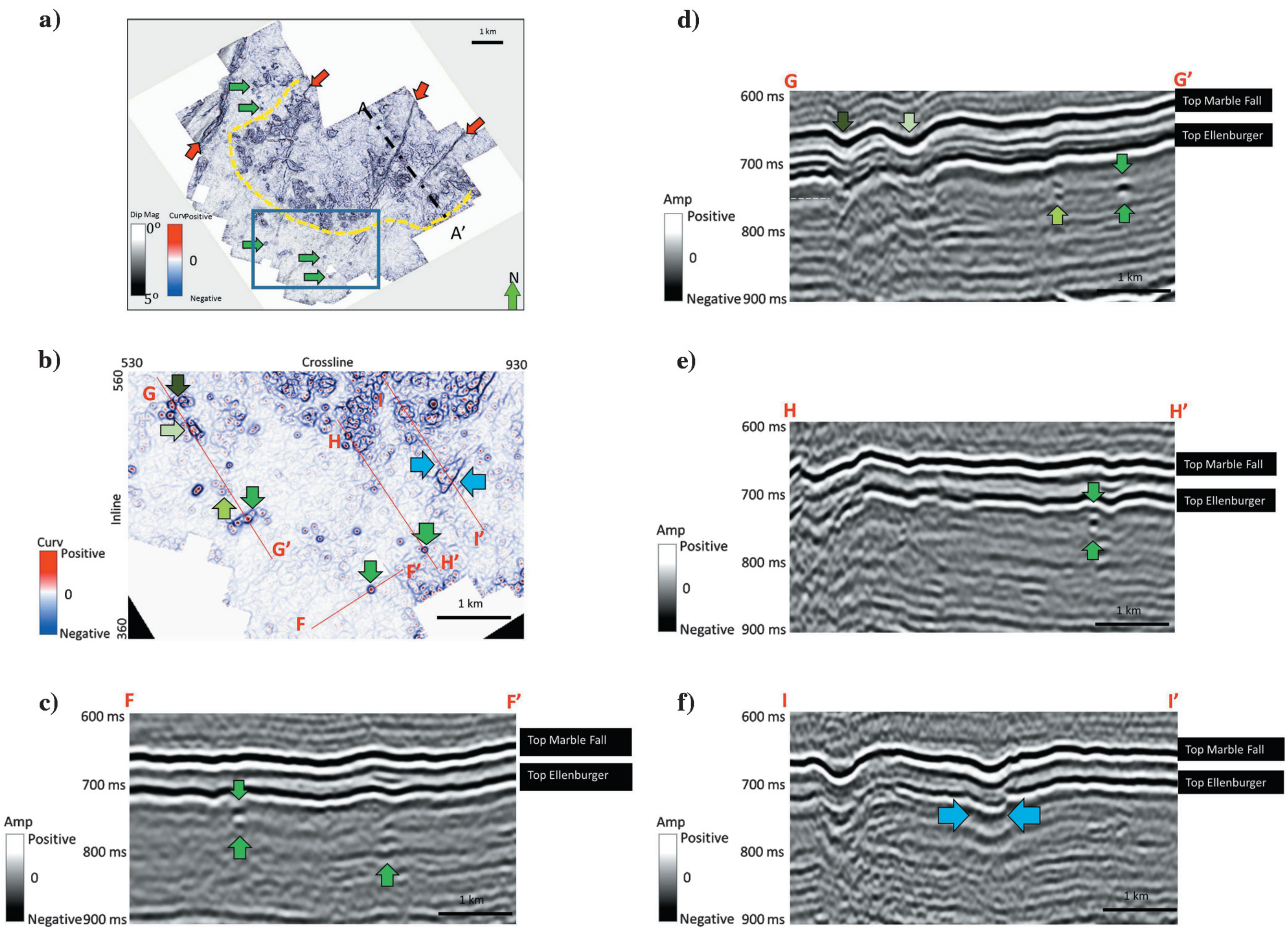

**Figure 18.** Time slice at $t = 0.750$ s through (a) most-negative amplitude curvature and (b) zoomed in zone, (c-f) are seismic section view of lines FF′, GG′, HH′, and II′. Circular collapse features are contained entirely within the Ellenburger Dolomite Formation and do not propagate shallower. Several of them exhibit the string-of-pearls pattern, suggesting that they are controlled by faults or joints.

and karst), the latter of which correlate to red, most-positive curvature and blue, most-negative structural curvature anomalies.

Figure 22 shows similar horizon slices but now through the amplitude curvature volume. As seen previously on the time slices, the amplitude curvature varies more rapidly laterally, likely indicating changes in impedance interpreted as variations in diagenetic alteration. Figure 22a and 22b shows the most-positive and most-negative amplitude curvature. Although these images are similar to Figure 21a and 21b, they indicate different concepts. The blue in the structural curvature indicates anomalously low structure, whereas the blue in the amplitude curvature indicates anomalously low amplitude. Thus, we observe lower reflectivity inside the structurally low-collapse features, which likely results from anomalous attenuation and/or scattering.

## Conclusions

Karst, faults, and joints are known to form geologic hazards for most Barnett Shale wells in the Fort Worth Basin. In the best cases, these drilling-related geohazards form conductive features that draw off expensive hydraulic fracturing fluid from the targeted shale formation. In the worst cases, the completed wells are hydraulically connected to the underlying Ellenburger aquifer and produce large amounts of water with little hydrocarbon. Three-dimensional seismic data are routinely acquired to map such geohazards prior to spudding. Such information should be presented during interdisciplinary, prespud meeting to alert the drilling and completion engineer of potential difficulties before finalization of the drilling and completion program.

Karst collapse generate a distinct morphologic pattern on 3D seismic data. When plotted using a gray scale, karst dolines appear on coherence and dip magnitude time slices as characteristically circular to elliptical features, which provide a karst "fingerprint." In this and many other surveys in the Fort Worth Basin,

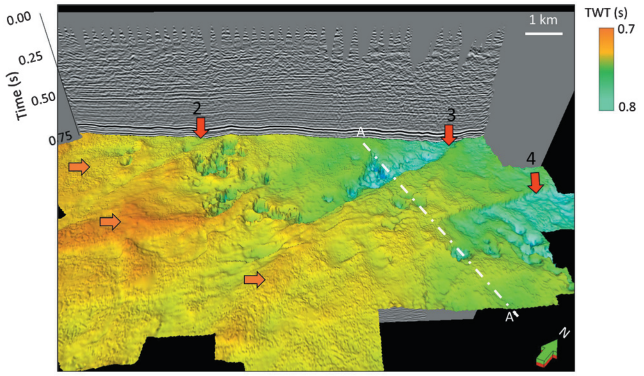

**Figure 20.** Time structure map of the top Ellenburger Group horizon. Karst collapse and three major faults are clearly seen. Note the increased rugosity of the surface toward the south and increased karst collapse toward the north. Orange arrows indicate a rugose surface. Red arrows indicate major faults.

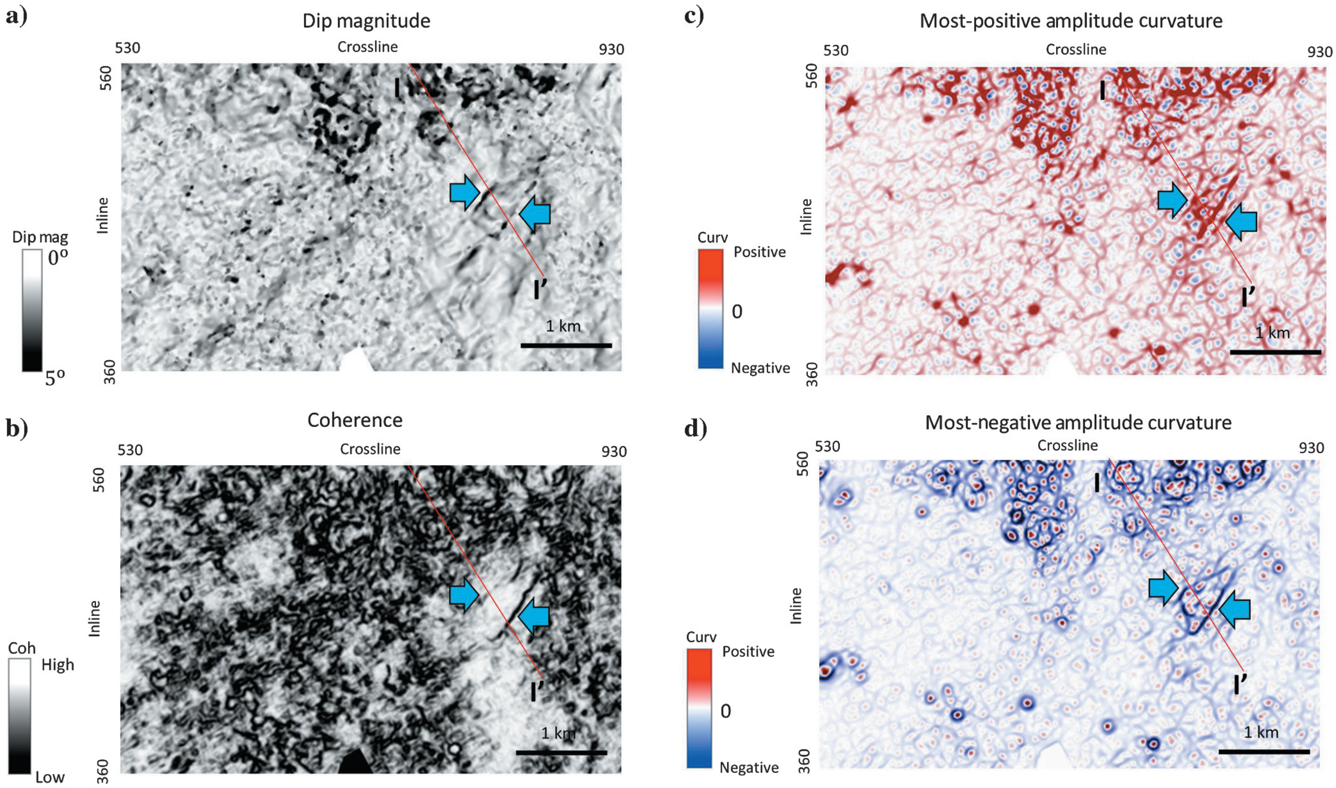

**Figure 19.** Time slice of zoomed in area at $t = 0.750$ s through the (a) dip magnitude, (b) coherence, (c) most-positive amplitude curvature, and (d) most-negative amplitude curvature. Note that the blue arrows indicate the subtle collapse-caused fault.

the karst are strongly correlated with fractures and joints, which in turn are clearly rendered on coherence and most-negative curvature images. The chaotic nature of reflectors internal to the karst features, such as paleocavern fill, often result in low-frequency anomalies. The loss of higher frequencies has two possible causes: the existence of fluid-filled fractures and cracks within the karst collapse features giving rise to intrinsic attenuation, and scattering from the chaotic infill giving rise to geometric attenuation. In this survey area, and throughout much of the Fort Worth Basin, wells that penetrate karst features or coincident fault and fracture system will produce water from the Ellenburger Group and thus, are not intentionally drilled.

Reflectors dip into the collapse features giving an inward radial display when dip azimuth is plotted against a cyclical-color bar. Vector convergence shows the complementary image, with reflectors converging outward toward the collapse edges. Reflectors at shallower levels in the Barnett Shale and Marble Falls intervals also show down warping into the karst but with parallel (nonconvergent) bedding and near constant thickness, implying that the actual collapse took place long after these formations were deposited. At the shallow Pennsylvanian-age Caddo horizon, the reflectors show strong negative curvature and dip magnitude anomalies, but no coherence anomalies, suggesting either delayed collapse or continued diagenetic alteration of the Ellenburger from below. Solution-enlarged joints and faults may remain partially open, or be fill with impermeable clays or preferentially cemented. In either case, they will give rise to lateral changes in amplitude measured by amplitude gradients and amplitude curvature. Karst-related architectural elements include dolines, paleocaverns, karst towers, solution-enlarged joints, and rugose topography that can inferred from attributes by integrating modern and ancient analogues, thereby providing mutually supportive lines of evidence for a compelling interpretation.

Time slices through seismic attributes provide a rapid yet quantitative delineation of karst terrains, delaying and perhaps circumventing the need to carefully pick the top of the difficult-to-pick Ellenburger unconformity. Indeed, many areas covered by 3D seismic data in the Fort Worth Basin have few wells, in which the engineers turn to less intensely karsted areas to complete.

Interpreters often wish to know which attribute is "best" to delineate a given geologic feature of interest. We propose using mathematically independent attributes, coupled through the underlying geology, to provide a means of confirming or rejecting a given interpretation hypothesis.

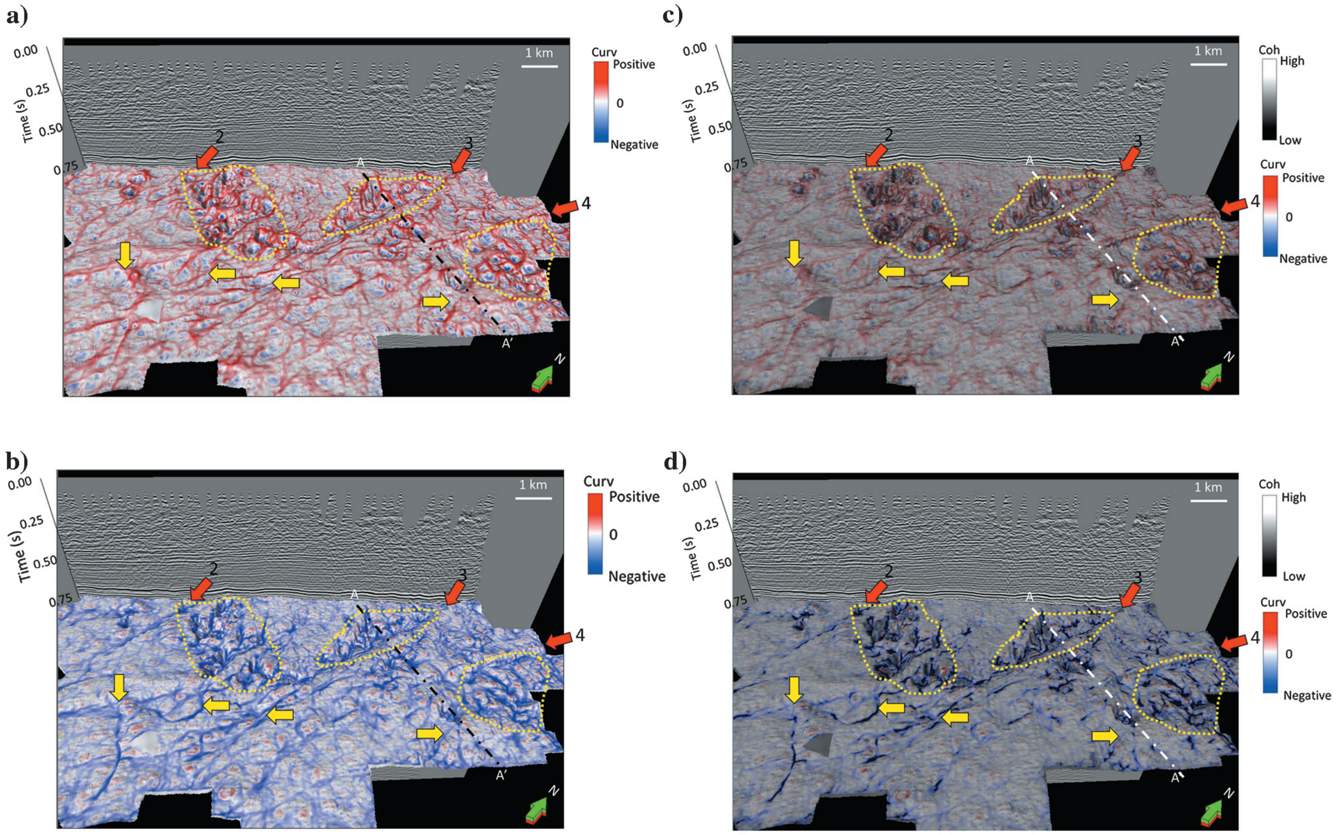

**Figure 21.** Vertical slice through seismic amplitude and horizon slices along the top Ellenburger Group horizon though the (a) most-positive and (b) most-negative structural curvature and (c) most-positive and (d) most-negative structural curvature corendered with coherence. Red arrows indicate major faults, and yellow dashed lines indicate where karst is developed and is larger than the other area where there are no major faults. Yellow arrows indicate surface folds and joints.

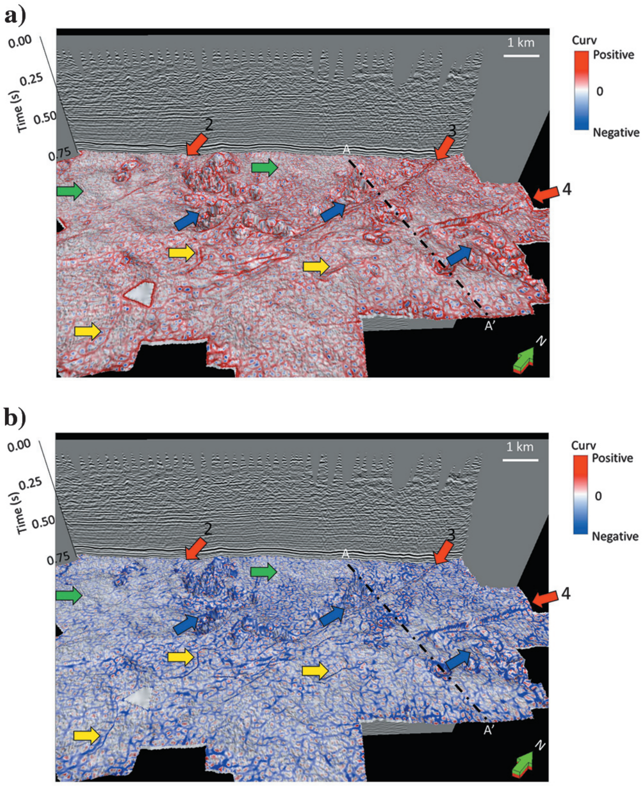

**Figure 22.** Vertical slice through seismic amplitude and horizon slices along the top Ellenburger Group horizon though the (a) most-positive and (b) most-negative amplitude curvature. Red arrows indicate major faults. Blue arrows indicate fault-controlled karst. Yellow arrows indicate surface folds and joints. The fractures are developed in zones where faults and karst are also developed. Green arrows indicate that the zones have no fault effects, so that fractures are not developed.

## Acknowledgments

The authors would like to thank Marathon Oil for providing the data and key insight in the data analysis of this region. We also thank J. Rush, Y. Sun, S. Chavez-Perez, and D. Herron for reviewing this manuscript and providing supportive comments. Financial support and most attribute computation was supported by the University of Oklahoma (OU) Attribute-Assisted Seismic Processing and Interpretation (Consortium). Data display was done using Petrel software provided to OU for use in research and education.

## Appendix A

## Simple definitions of attributes and operations used

In this appendix, we summarize several of the seismic attributes used in the paper. Several of these definitions are extracted from the glossary in Chopra and Marfurt (2007), which in turn were adapted from definitions in Sheriff (2002). Much greater detail can be found at http://geology.ou.edu/aaspi/documentation/.

### Apparent inline dip

For time-migrated data, the apparent dip is the change in reflector time from with respect to distance in a given direction and is measured in units of s/m. Using the SEGY convention, in which the $y$-axis is north and the $x$-axis is east, the apparent north component of dip $p_y$ and the east component of dip $p_x$ are given by

$$p_x = \frac{\partial t}{\partial x}, \tag{A-1}$$

and

$$p_y = \frac{\partial t}{\partial y}. \tag{A-2}$$

In our examples, we computed the inline and crossline components of dip using a multiwindow Kuwahara semblance search technique described by Marfurt (2006). The apparent dip in the ξ-direction (in this paper, 0°, 45°, 90°, and 135° from north) is

$$p_\xi = \frac{\partial t}{\partial \xi} = (\cos\xi)p_y + (\sin\xi)p_x. \tag{A-3}$$

### Dip magnitude and dip azimuth

The dip magnitude is measured in s/m and $|\mathbf{p}|$ is the magnitude of the vector dip $\mathbf{p}$ given by

$$|\mathbf{p}| = (p_x^2 + p_y^2)^{1/2}. \tag{A-4}$$

Conversion to angular dip $\theta$ requires the use of a velocity $V_\mathrm{P}$, which we set to 15,000 ft/s, representative of the Barnett Shale and Ellenburger Dolomite, and it is given by

$$\theta = \tan^{-1}\left[\frac{V_\mathrm{P}}{2}(p_x^2 + p_y^2)^{1/2}\right]. \tag{A-5}$$

The dip azimuth from north is

$$\psi = \mathrm{ATAN2}(p_y, p_x), \tag{A-6}$$

where ATAN2 produces a result that ranges between $-180^0$ and $+180^0$.

### Coherence

Coherence is a measure of waveform similarity. In our examples, we estimate the coherence of $J$ traces within a $\pm K$ sample analysis window as the ratio between the coherent energy within an analysis window to the total energy within the analysis window:

$$c = \frac{\sum_{k=-K}^{+K}\left[\sum_{j=1}^{J}(d_j^{\mathrm{coh}})^2\right]}{\sum_{k=-K}^{+K}\left[\sum_{j=1}^{J}(d_j^{\mathrm{orig}})^2\right]}. \tag{A-7}$$

Semblance-based coherence estimates the coherent part of the data by the average trace within the analysis window. In the examples we show here, we estimate the coherent part of data using a Karhunen-Loeve filter. We always compute coherence along the structural dip.

### Structure-oriented filter

As the name implies, SOF is computed along structural dip as estimated by equations A-1 and A-2. Our implementation builds on other previously computed components. First, we examine the centered window and examine its coherence. If the coherence is below a given threshold (e.g., $c < 0.6$), then we do not filter the data in an attempt to preserve a potential "edge." If the coherence is above the threshold, we compare this value with the coherence of all noncentered analysis windows that includes the voxel of interest and choose the one with the highest coherence value. Within this window, we apply a Karhunen-Loeve filter and output the filtered sample value.

### Spectral components

In this paper, we computed spectral components using a matching pursuit algorithm described by Liu and Marfurt (2007). We begin by computing a library of complex Ricker wavelets. Then, we compute the instantaneous envelope and frequency of a given trace. Then, using a user-defined threshold (in our examples $r = 0.8$), we extract the time and instantaneous frequency of all envelopes that exceed $r$ times the largest envelope. Wavelets of unknown complex amplitude $\alpha$ (or alternatively, unknown magnitude and phase) for the given instantaneous (average) frequency are then extracted from the dictionary. The values of $\alpha$ are computed using least-squares, scaled complex spectra from the dictionary are accumulated and the residual trace is generated. This process iterates until the residual energy is a small percentage of the energy of the original trace. The result is a time-frequency spectral decomposition with a spectrum at each time sample.

The peak magnitude is the maximum magnitude at a given voxel and the peak frequency the corresponding frequency of the spectrum.

### Spectral balancing and spectral bluing

Given the spectra at every voxel, we compute the average time-frequency spectra for the entire survey. After some vertical smoothing (±0.2 s in our example), we balance the spectra using

$$a_j^{\text{blue}}(t,f) = \left[\frac{P_{\text{peak}}(t)}{P_{\text{avg}}(t,f) + \varepsilon P_{\text{peak}}(t)}\right]^{1/2} f^{\beta} a_j(t,f), \quad \text{(A-8)}$$

where $a_j(t,f)$ is the magnitude spectrum of the $j$th trace computed using spectral decomposition, $P_{\text{avg}}(t,f)$ is the smoothed, average power spectrum for the entire survey, $P_{\text{peak}}(t)$ is the peak power of the smoothed average power spectrum at time $t$, $\varepsilon = 0.01$ is a prewhitening factor, and $\beta = 0.3$ is a bluing factor described by Neep (2007). After balancing and bluing the magnitude spectra, the balanced and blued output trace is reconstructed by adding its complex (modified magnitude and unchanged phase) components.

### Structural curvature

There is considerable confusion in terms of curvature definitions. Mathematically, the curvature is based on eigenvector analysis. In this definition, the maximum curvature is that curvature that best represents the deformation at a given voxel. If that best representation is a syncline, the maximum curvature happens to be negative and the corresponding minimum curvature that represents the least deformation at a voxel will have a larger signed value. Because most geophysicists do not live in eigenvector space, this nomenclature is not used by approximately 50% of the commercial curvature software implementations, who propose that the maximum curvature should have a greater than or equal signed value as the minimum curvature. We avoid this confusion by explicitly defining the most-positive and most-negative principal (i.e., eigenvector) curvatures, where $k_1 \geq k_2$. We compute volumetric curvature as the first derivatives of the volumetric north and east apparent components of dip. The long-wavelength versions we compute are band-pass-filtered versions of the curvature results, though using the associative law of linear operators, it is computationally more convenient to band pass filter the derivative operators rather than the output curvature result. Details of this implementation can be found in Chopra and Marfurt (2007).

### Amplitude gradients

Mathematically, amplitude gradients are like time-structure gradients. Within an analysis window, we compute the Karhunen-Loeve filtered version of the data, which has an associated eigenvalue $\lambda$, and eigenvector (actually, in 2D, an eigenmap) $v(x,y)$, which has a magnitude of 1.0. The east and north components of the energy-weighted (i.e., the eigenvalue weighted) amplitude gradient $\mathbf{g}$ are then

$$g_x = \lambda \frac{\partial v}{\partial x}, \quad \text{(A-9)}$$

and

$$g_y = \lambda \frac{\partial v}{\partial y}. \quad \text{(A-10)}$$

Amplitude gradients always need to be computed along structural dip. One can also compute impedance gradients.

### Amplitude curvature

Although structural curvature is computed by taking the first derivatives of structural dip, amplitude curvature is computed by taking the first derivatives of the amplitude gradient. In our implementation, we apply the same long-wavelength filter operators as we do in structural curvature. The major difference is that the vertical dimension is different in amplitude curvature, such that we compute the mathematically simpler most-positive and most-negative amplitude curvatures (without the word principal). This simple calculation delineates zones that have extreme values of energy and in our examples shows joints and collapse features. Amplitude curvature can also be computed from impedances or any other gradient attribute.

### Structure rotation and convergence

Geophysicists familiar with fluid mechanics and electromagnetics are comfortable with taking the divergence and curl of vectors. The divergence of the structural dip vector is twice the mean curvature. The curl of vector dip is in turn a vector. Computationally, it is convenient to convert from the dip vector **p**, to the normal vector **n**. Marfurt and Rich (2010) then define the structural rotation (the $z$-component of the curl vector) as

$$r = n_x\left(\frac{\partial n_y}{\partial z} - \frac{\partial n_z}{\partial y}\right) - n_y\left(\frac{\partial n_z}{\partial x} - \frac{\partial n_x}{\partial z}\right) - n_z\left(\frac{\partial n_x}{\partial y} - \frac{\partial n_y}{\partial x}\right), \tag{A-11}$$

and the structural convergence (the $x$- and $y$-components of the curl vector)

$$\begin{aligned} \mathbf{C} = {} & \hat{x}\left[n_x\left(\frac{\partial n_x}{\partial y} - \frac{\partial n_y}{\partial x}\right) - n_z\left(\frac{\partial n_y}{\partial z} - \frac{\partial n_z}{\partial y}\right)\right] \\ & + \hat{y}\left[n_z\left(\frac{\partial n_y}{\partial z} - \frac{\partial n_z}{\partial y}\right) - n_x\left(\frac{\partial n_x}{\partial y} - \frac{\partial n_y}{\partial x}\right)\right] \\ & + \hat{z}\left[n_x\left(\frac{\partial n_z}{\partial x} - \frac{\partial n_x}{\partial z}\right) - n_y\left(\frac{\partial n_y}{\partial z} - \frac{\partial n_z}{\partial y}\right)\right], \end{aligned} \tag{A-12}$$

where the ^ denotes the unit normal. As with curvature, we have chosen to apply a long-wavelength filter to these derivative operators. Furthermore, the components of curl are best projected along axes perpendicular to the average local dip rather than along the vertical. Rotation enhances measures the rotation of reflector dip rotation fault planes, but is also sensitive to lateral changes in accommodation space and lateral changes in angular unconformities. Convergence is a 2D vector and shows the magnitude and azimuth of convergence, such as occurs with pinch outs and angular unconformities.

## References

Al-Dossary, S., and K. J. Marfurt, 2006, 3D volumetric multispectral estimates of reflector curvature and rotation: Geophysics, **71**, no. 5, P41–P51, doi: 10.1190/1.2242449.

Bahorich, M. S., and S. L. Farmer, 1995, 3D seismic discontinuity for faults and stratigraphic features: The coherence cube: 65th Annual International Meeting, SEG, Expanded Abstracts, 93–96.

Bruner, K. R., and R. Smosna, 2011, A comparative study of the Mississippian Barnett Shale, Fort Worth basin, and Devonian Marcellus Shale, Appalachian basin: Technical Report DOE/NETL/2011/1478, National Energy Technology Laboratory for the United States Department of Energy.

Chen, M., S. Zhan, Z. Wan, H. Zhang, and L. Li, 2010, Detecting carbonate-karst reservoir using the directional amplitude gradient difference technique: 81st Annual International Meeting, SEG, Expanded Abstracts, 1845–1849.

Chopra, S., and K. J. Marfurt, 2007, Volumetric curvature attributes add value to 3D seismic data interpretation: The Leading Edge, **26**, 856–867, doi: 10.1190/1.2756864.

Duo, Q., Y. Sun, C. Sullivan, and H. Guo, 2011, Paleokarst system development in the San Andres Formation, Permian Basin, revealed by seismic characterization: Journal of Applied Geophysics, **75**, 379–389, doi: 10.1016/j.jappgeo.2011.08.003.

Elebiju, O. O., G. R. Keller, and K. J. Marfurt, 2010, Case history investigation of links between Precambrian basement structure and Paleozoic strata in the Fort Worth basin, Texas, USA, using high-resolution aeromagnetic, HRAM data and seismic attributes: Geophysics, **75**, no. 4, B157–B168, doi: 10.1190/1.3435939.

Feng, X., Y. Wang, X. Wang, N. Wang, G. Gao, and X. Zhu, 2012, The application of high-resolution 3D seismic acquisition techniques for carbonate reservoir characterization in China: The Leading Edge, **31**, 168–179, doi: 10.1190/1.3686914.

Ferrill, D. A., and A. P. Morris, 2008, Fault zone deformation controlled by carbonate mechanical stratigraphy, Balcones fault system, Texas: AAPG Bulletin, **92**, 359–380, doi: 10.1306/10290707066.

Gale, J. F. W., R. M. Reed, and J. Holder, 2007, Natural fractures in the Barnett Shale and their importance for hydraulic fracture treatments: AAPG Bulletin, **91**, 603–622, doi: 10.1306/11010606061.

Hardage, B., D. Carr, D. Lancaster, J. Simmons, Jr., R. Elphick, V. Pendleton, and R. Johns, 1996, 3D seismic evidence of the effects of carbonate karst collapse on overlying clastic stratigraphy and reservoir compartmentalization: Geophysics, **61**, 1336–1350, doi: 10.1190/1.1444057.

Holtz, M. H., and C. Kerans, 1992, Characterization and categorization of West Texas Ellenburger reservoirs, *in* M. P. Candelaria, and C. L. Reed, eds., Paleokarst, karst related diagenesis and reservoir development: Examples from Ordovician-Devonian age strata of West Texas and the Mid-Continent: Permian Basin Section SEPM Publication, 31–44.

Kerans, C., 1988, Karst-controlled reservoir heterogeneity in Ellenburger Group carbonates of West Texas: Reply: AAPG Bulletin, **72**, 1160–1183.

Kerans, C., 1989, Karst-controlled reservoir heterogeneity and an example from the Ellenburger group (Lower Ordovician) of West Texas: The University of Texas at Austin, Bureau of Economic Geology Report of Investigations.

Kerans, C., 1990, Depositional systems and karst geology of the Ellenburger Group (Lower Ordovician), subsurface West Texas: The University of Texas at Austin, Bureau of Economic Geology Report of Investigations.

Khatiwada, M., G. R. Keller, and K. J. Marfurt, 2013, A window into the Proterozoic: Integrating 3D seismic, gravity and magnetic data to image subbasement structures in the southeast Fort Worth basin: Interpretation, **1**, no. 2, T125–T141, doi: 10.1190/INT-2013-0041.1.

Leach, D. L., and D. F. Sangster, 1993, Mississippi Valley-type lead-zinc deposits: Geological Association of Canada.

Liu, J., and K. J. Marfurt, 2007, Instantaneous spectral attributes to detect channels: Geophysics, **72**, no. 2, P23–P31, doi: 10.1190/1.2428268.

Liu, Y., X. Liang, and Y. Zhou, 2011, A method of acquiring full azimuth data for carbonate reservoirs exploration in Tarim basin, western China: 82nd Annual International Meeting, SEG, Expanded Abstracts, doi: 10.1190/segam2012-0005.1.

Loucks, R. G., 2003, Understanding the development of breccias and fractures in Ordovician carbonate reservoirs, *in* T. J. Hunt, and P. H. Lufholm, eds., The Permian Basin: Back to basics: West Texas Geological Society Fall Symposium: West Texas Geological Society, 231–252.

Loucks, R. G., 2008, Review of the lower Ordovician Ellenburger group of the Permian basin, West Texas, http://www.beg.utexas.edu/resprog/permianbasin/PBGSP_members/writ_synth/Ellenburger%20report.pdf, accessed 8 September 2012.

Lucia, F. J., 1971, Lower Paleozoic history of the western Diablo Platform, West Texas and south-central New Mexico, *in* J. M. Cys, ed., Robledo Mountains and Franklin Mountains — 1971 Field Conference Guidebook: Permian Basin Section, SEPM, 174–219.

Lucia, F. J., 1995, Lower Paleozoic cavern development, collapse, and dolomitization, Franklin Mountains, El Paso, Texas, *in* D. A. Budd, A. H. Saller, and P. M. Harris, eds., Unconformities and porosity in carbonate strata: AAPG Memoir 63, 279–300.

Marfurt, K. J., 2006, Robust estimates of 3D reflector dip and azimuth: Geophysics, **71**, no. 4, P29–P40, doi: 10.1190/1.2213049.

Marfurt, K. J., and J. R. Rich, 2010, Beyond curvature: Volumetric estimates of reflector rotation and convergence: 80th Annual International Meeting, SEG, Expanded Abstracts, 1467–1472.

McDonnell, A., R. G. Loucks, and T. Dooley, 2007, Quantifying the origin and geometry of circular sag structures in northern Fort Worth Basin, Texas: Paleocave collapse, pull-apart fault systems, or hydrothermal alteration?: AAPG Bulletin, **91**, 1295–1318, doi: 10.1306/05170706086.

Neep, J. P., 2007, Time-variant colored inversion and spectral blueing: 69th Annual International Conference and Exhibition, EAGE, Extended Abstracts, E044.

Partyka, G. A., J. A. Gridley, and J. A. Lopez, 1999, Interpretational applications of spectral decomposition in reservoir characterization: The Leading Edge, **18**, 353–360, doi: 10.1190/1.1438295.

Pollastro, R. M., D. M. Jarvie, R. J. Hill, and C. W. Adams, 2007, Geologic framework of the Mississippian Barnett shale, Barnett-paleozoic total petroleum system, Bend arch — Fort Worth Basin, Texas: AAPG Bulletin, **91**, 405–436, doi: 10.1306/10300606008.

Qi, J., and J. P. Castagna, 2013, Application of a PCA fault-attribute and spectral decomposition in Barnett shale fault detection: 83rd Annual International Meeting, SEG, Expanded Abstracts, 1421–1425.

Roende, H., C. Meeder, J. Allen, S. Peterson, and D. Eubanks, 2008, Estimating subsurface stress direction and intensity from subsurface full azimuth land data: 78th Annual International Meeting, SEG, Expanded Abstracts, 217–220.

Roth, M., and A. Thompson, 2009, Fracture interpretation in the Barnett Shale using macro and microseismic data: First Break, **27**, 61–65.

Schuelke, J. S., 2011, Overview of seismic attribute analysis in shale play: Attributes: New views on seismic imaging: Their use in exploration and production: Presented at 31st Annual GCSSEPM Foundation Bob F. Perkins Research Conference.

Sheriff, R. E., 2002, Encyclopedic dictionary of applied geophysics, 4th ed.: SEG.

Sullivan, E., K. Marfurt, and M. Ammerman, 2003, Bottoms up karst: New 3D seismic attributes shed light on the Ellenburger (Ordovician) carbonates in the Fort Worth Basin (north Texas, USA): 73rd Annual International Meeting, SEG, Expanded Abstracts, 482–485.

Sullivan, E. C., K. J. Marfurt, A. Lacazette, and M. Ammerman, 2006, Application of new seismic attributes to collapse chimneys in the Fort Worth basin: Geophysics, **71**, no. 4, B111–B119, doi: 10.1190/1.2216189.

Wang, F. P., and J. F. W. Gale, 2009, Screening criteria for shale-gas systems: GCAGS Transactions, **59**, 779–793.

---

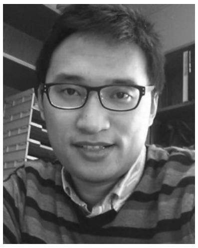

**Jie Qi** is a Ph.D. student in geophysics and a research assistant at the University of Oklahoma, Norman, USA. He received an M.D. from the University of Houston, Texas, USA, and a B.D. from the China University of Petroleum, Beijing, China. In 2011, he studied at the University of Houston, and he also worked as a research assistant in spectral decomposition and seismic interpretation. His research interests include seismic attribute analysis, seismic inversion, signal processing, modeling, and migration.

He is a member of SEG, AAPG, and the Geophysical Societies of Houston. His current research includes seismic attribute analysis, geologic features interpretation on 3D seismic data, and prestack imaging.

**Bo Zhang** received a B.S. (2006) in Geophysics from China University of Petroleum, and an M.S. (2009) in Geophysics from the Institute of Geology and Geophysics, Chinese Academy of Sciences. He is currently a doctoral student at the University of Oklahoma and the thesis title is long offset seismic analysis for resources plays.

**Huailai Zhou**is an associate professor of College of Geophysics, in Chengdu University of Technology, and postdoctor. He received his PHD degree in Earth Exploration and Information Techniques, from Chengdu University of Technology in 2009. He completed the postdoctoral research with Institute of Sedimentary Geology in Chengdu University of Technology from 2010 to 2012. He is sponsored by China Scholarship Council to work as postdoctoral research faculty in the University of Oklahoma, USA, from October 2013 to October 2014. His research work is mainly focused on research of seismic data processing methods, seismic modeling and imaging by wave equation numerical method, inversion and reservoir prediction.

**Kurt J. Marfurt** joined The university of Oklahoma in 2007, where he serves as the Frank and Henrietta Schultz Professor of Geophysics within the ConocoPhillips School of Geology and Geophysics. His primary research interests include development and calibration of new seismic attributes to aid in seismic processing, seismic interpretation, and reservoir characterization. Recent work has focused on correlating seismic attributes such as volumetric curvature, impedance inversion, and azimuthal anisotropy with image logs and microseismic measurements with a particular focus on resource plays. In addition to teaching and research duties at OU, he leads short courses on attributes for SEG and AAPG.